Bioactive Materials 56 (2026) 248–259

Contents lists available at ScienceDirect

Bioactive Materials

journal homepage: www.keaipublishing.com/en/journals/bioactive-materials

Metal fluoride nanoregulators reverse therapeutic resistance via stemness remodeling to trigger pyroptosis for chemoimmunotherapy

Shumin Sun [a], Nailin Yang [a,b,*], Jihu Nie [a], Linzhu Zhang [a], Di Wang [a,c], Xingwei Sun [c,**], Yong Jin [c], Liang Cheng [a,b,***]

[a] Institute of Functional Nano & Soft Materials (FUNSOM), Jiangsu Key Laboratory for Carbon-Based Functional Materials and Devices, Soochow University, Suzhou, 215123, China
[b] Macao Institute of Materials Science and Engineering, Macau University of Science and Technology, Taipa, 999078, Macau SAR, China
[c] Department of Intervention, The Second Affiliated Hospital of Soochow University, Suzhou, 215004, China

ARTICLE INFO

Keywords:
Chemoimmunotherapy
Cancer stem cells
Wnt/β-catenin signaling
Pyroptosis
Bioactive materials

ABSTRACT

Chemoresistance and immunosuppression serve as major obstacles that compromise the therapeutic efficacy of chemoimmunotherapy. Herein, we reported a novel chemoimmunotherapy strategy employing metal fluoride to modulate Wnt/β-catenin signaling, effectively remodeling treatment resistance and eliciting pyroptosis-mediated immune activation. Through systematic screening of various nonmetallic anions (F^-, Cl^-, Br^-, I^-, CO_3^{2-}, PO_4^{3-}, S^{2-}, and Se^{2-}), we identified F^- as an effective inhibitor of β-catenin expression and tumor stemness. The synergistic combination of F^- with chemotherapy significantly attenuated tumor stemness and enhanced treatment efficacy. We further engineered 5-Fu@FeF_2 nanomedicine (FFN-5) and investigated its chemoimmunotherapeutic effects. FFN-5 potently suppressed β-catenin expression, effectively diminishing cancer stemness while augmenting the cytotoxicity of 5-Fu, ultimately triggering pyroptosis. Local administration of FFN-5 not only inhibited tumor growth but also remodeled the immunosuppressive tumor microenvironment (TME), thereby promoting antitumor immunity. When combined with immune checkpoint blockade (ICB), this combined approach triggered a potent systemic immune response, effectively controlling both primary and distant lesions. Furthermore, the unique stemness-modulating properties of F-based nanomodulators significantly suppressed tumor metastasis. In summary, we demonstrated that F^- effectively suppressed tumor stemness, and developed an innovative FFN-5 nanoplatform that enhanced chemoimmunotherapy by modulating stemness-dependent cell death mechanisms, suggesting a promising strategy to overcome resistance to cancer treatment.

1. Introduction

Colorectal cancer (CRC), which holds the position of the third most common occurring malignant tumor worldwide, persists as a major contributor to cancer-related deaths due to its high recurrence rate and propensity for distant metastasis [1]. Characterized by insidious progression and frequent late-stage diagnosis, CRC often requires intensive therapeutic approaches, including surgery, radiation, and chemotherapy [2]. Among these, chemotherapeutic agents such as 5-fluorouracil (5-Fu) remain cornerstone treatments. However, therapeutic efficacy is significantly hampered by acquired drug resistance, with nearly 50 % of patients developing tumor recurrence [3,4]. This drug resistance is closely associated with tumor heterogeneity, which is linked to cancer stem cells (CSCs), a rare subpopulation that demonstrates self-renewal capacity, pluripotency, and enhanced survival mechanisms under therapeutic stress [5–8]. CSCs are critically regulated

Peer review under the responsibility of editorial board of Bioactive Materials.
* Corresponding author. Institute of Functional Nano & Soft Materials (FUNSOM), Jiangsu Key Laboratory for Carbon-Based Functional Materials and Devices, Soochow University, Suzhou, 215123, China.
** Corresponding author. Department of Intervention, The Second Affiliated Hospital of Soochow University, Suzhou, 215004, China.
*** Corresponding author. Institute of Functional Nano & Soft Materials (FUNSOM), Jiangsu Key Laboratory for Carbon-Based Functional Materials and Devices, Soochow University, Suzhou, 215123, China.
E-mail addresses: nlyang@suda.edu.cn (N. Yang), 20184133174@suda.edu.cn (X. Sun), lcheng2@suda.edu.cn (L. Cheng).

https://doi.org/10.1016/j.bioactmat.2025.10.011
Received 9 August 2025; Received in revised form 1 October 2025; Accepted 12 October 2025
2452-199X/© 2025 The Authors. Publishing services by Elsevier B.V. on behalf of KeAi Communications Co. Ltd. This is an open access article under the CC BY-NC-ND license (http://creativecommons.org/licenses/by-nc-nd/4.0/).

by dynamic interactions within the tumor microenvironment (TME), particularly through the Wnt/β-catenin signaling pathway [9,10]. As a central mediator of CSC niche maintenance, aberrant activation of β-catenin not only promotes tumor initiation and progression but also fosters an immunosuppressive TME that evades anti-tumor immune responses [11,12]. Therefore, targeting Wnt/β-catenin signaling has emerged as a promising therapeutic strategy to disrupt CSC plasticity and improve treatment efficacy [13,14]. Nevertheless, existing stemness-targeted therapies often fail to achieve complete tumor eradication, leaving residual lesions that may fuel CSC regeneration and metastatic outgrowth [15,16]. These challenges underscore the urgent need for innovative interventions capable of synergistically suppressing oncogenic signaling pathways while ensuring precise tumor elimination.

The advent of immunotherapy, particularly immune checkpoint blockade (ICB), has redefined therapeutic paradigms for malignancies over the past decade [17–21]. Despite achieving clinically meaningful outcomes across multiple tumor types, durable ICB responses remain confined to a minority of patients. This has facilitated advancements in integrated treatment strategies that combine chemotherapy and immunotherapy, referred to as chemoimmunotherapy [22–25]. Paradoxically, CRC presents challenges due to its intrinsically immunosuppressive nature, manifested by inadequate cytotoxic T lymphocyte (CTL) infiltration and blunted immunogenic responses [26]. Conventional chemotherapeutics predominantly eliminate malignant cells through immunologically silent apoptosis, wherein rapid clearance of apoptotic debris by phagocytes fails to elicit therapeutic immune activation [27,28]. In contrast, pyroptosis, an immunostimulatory variant of lytic programmed cell death, has emerged as a transformative strategy in cancer immunotherapy through its dual capacity to anesthetize immunosuppressive tumor niches and ignite systemic immune surveillance [29–33]. Capitalizing on this principle, recent advances in nanobiotechnology have enabled the engineering of tumor-targeted nanomaterials capable of precise pyroptosis induction, thereby converting "cold" CRC tumors into immunologically "hot" phenotypes [34–38]. Therefore, there is an urgent need to devise chemotherapeutic strategies that can shift tumor cell death from apoptosis to pyroptosis, thereby augmenting tumor immunogenicity. However, certain resistance mechanisms within the tumor inhibit the induction of immunogenic cell death (ICD). Emerging studies have demonstrated that dysregulated Wnt/β-catenin signaling not only mediates chemoresistance but also selectively shields malignant cells from diverse ICD modalities such as cuproptosis and ferroptosis, ultimately suppressing therapy-driven immune activation [39–41]. β-catenin suppresses pyroptosis by inhibiting the expression of the NLRP3 protein and the assembly of the NLRP3 inflammasome [42]. These findings imply that Wnt/β-catenin pathway inhibition could concurrently counteract drug resistance mechanisms, reprogram cell death mechanisms, and provoke immunostimulatory effects.

Nutrient elements play pivotal roles in augmenting immune function and disease resistance, driving significant advancements in ion-based immunotherapy with particular emphasis on metalloimmunotherapy [43–45]. Current research reveals two principal mechanisms for ion-enhanced antitumor immunity: directly modulating the phenotype and function of immune cells, and indirectly regulating the immune response through the modulation of cancer cell death modes. Key findings demonstrate that specific ions regulate immune cell functions through multiple pathways: enhancing T-cell activation and effector functions (e.g., Na^+, Mg^{2+}), modulating macrophage polarization and metabolic reprogramming (e.g., K^+, Cu^{2+}), and potentiating cGAS-STING signaling activation (e.g., Mn^{2+}, Co^{2+}) [46–51]. Moreover, ionic components influence various cell types of death modalities, including pyroptosis (e.g., Zn^{2+} and Sb^{3+}), ferroptosis (Fe^{2+}), cuproptosis (e.g., Cu^{2+}), and PANoptosis (e.g., synergistic coordination of Cu^{2+} and Zn^{2+}) [52–57]. Therefore, the integration of nutritional ionic components into nanotherapeutic platforms presents a promising frontier in oncology treatments. However, current investigations into non-metallic ionic species remain preliminary, particularly regarding their regulatory effects on CSCs. The advancement of ion-based nanomedicines capable of modulating CSCs presents considerable promise and transformative implications, as these agents may improve chemosensitivity while concurrently modulating cell death modalities to bolster immune responses.

Herein, we present an advanced cancer chemoimmunotherapy platform utilizing metal fluoride nanomedicines as Wnt/β-catenin signaling modulators to overcome therapeutic resistance while triggering pyroptosis-mediated antitumor immunity (Scheme 1). Briefly, we screened the regulatory potential of various nonmetallic ions (F^-, Cl^-, Br^-, I^-, CO_3^{2-}, PO_4^{3-}, S^{2-}, and Se^{2-}) on tumor stemness and identified F^- as a potent suppressor of β-catenin expression. Mechanistically, F^- inhibited the pathway by upregulating Dickkopf-1 (DKK1), which promoted β-catenin entry into the phosphorylation-dependent degradation pathway, thereby reducing its protein levels. The synergistic combination of F^- with chemotherapy significantly attenuated tumor stemness and improved therapeutic outcomes. Based on these findings, we engineered 5-Fu@FeF_2 nanomedicine (FFN-5) and comprehensively analyzed its chemoimmunotherapeutic synergy. Notably, FeF_2 substantially diminished cell stemness by effectively downregulating the expression of β-catenin and significantly potentiated the cytotoxic effects of 5-Fu on cancer cells, thereby inducing pyroptosis in tumor cells. The intratumoral administration of FFN-5 effectively suppressed tumorigenesis and triggered pyroptosis, thereby converting the immunosuppressive TME towards a more favorable state for the immune response. Therefore, the integration of this innovative strategy with ICB treatment elicited a robust systemic immune response, effectively restraining both primary and distant tumors. Moreover, the exceptional stemness regulation capabilities of F-based nanomodulators substantially inhibited tumor metastasis. Collectively, we validated the regulatory potential of F in modulating tumor stemness and developed a novel FFN-5 platform for chemoimmunotherapy, demonstrating that stemness manipulation can dictate cell death mechanisms to potentiate therapy.

2. Results and discussion

2.1. Screening of nonmetallic ions for tumor stemness inhibition

The oncogenic transcription factor β-catenin, a key mediator of Wnt signaling, is critically involved in the pathogenesis of multiple malignancies, including colorectal, breast, and lung cancers [11]. First, to investigate its involvement in CRC, we assessed β-catenin expression in clinical samples, including adjacent normal tissue, primary tumor tissue, and post-chemotherapy residual tumor tissue (Fig. 1a and b). Notably, tumor tissues exhibited significantly higher β-catenin levels compared to normal adjacent tissues, with a further increase following chemotherapy, suggesting a potential link between β-catenin upregulation and chemoresistance. To explore therapeutic strategies targeting β-catenin, we systematically assessed the effects of various nonmetallic ions (F^-, Cl^-, Br^-, I^-, CO_3^{2-}, PO_4^{3-}, S^{2-}, and Se^{2-}) on β-catenin protein expression. Strikingly, fluoride (F^-) treatment led to pronounced downregulation of β-catenin (Fig. 1c–e; Fig. S1), indicating its potential as a novel ionic therapeutic agent for immunotherapy. Western blot (WB) analysis further corroborated these findings, confirming the efficient suppression of β-catenin by F^- (Fig. 1f; Fig. S3). In contrast, the β-catenin antagonist DKK1 exhibited an inverse expression pattern in CRC tissues, with reduced levels in tumors and further suppression after chemotherapy (Fig. 1g and h). Intriguingly, F^- treatment not only diminished β-catenin but also concurrently upregulated DKK1 expression (Fig. 1i–k; Fig. S2). WB analysis further validated the upregulation of DKK1 after treatment with F^- (Fig. 1l; Fig. S3). Moreover, time-course experiments revealed that F^- exerted a time-dependent inhibitory effect on β-catenin while increasing DKK1 expression (Fig. S4). Furthermore, the phosphorylation of β-catenin exhibited a concentration-dependent increase (Fig. 1m).

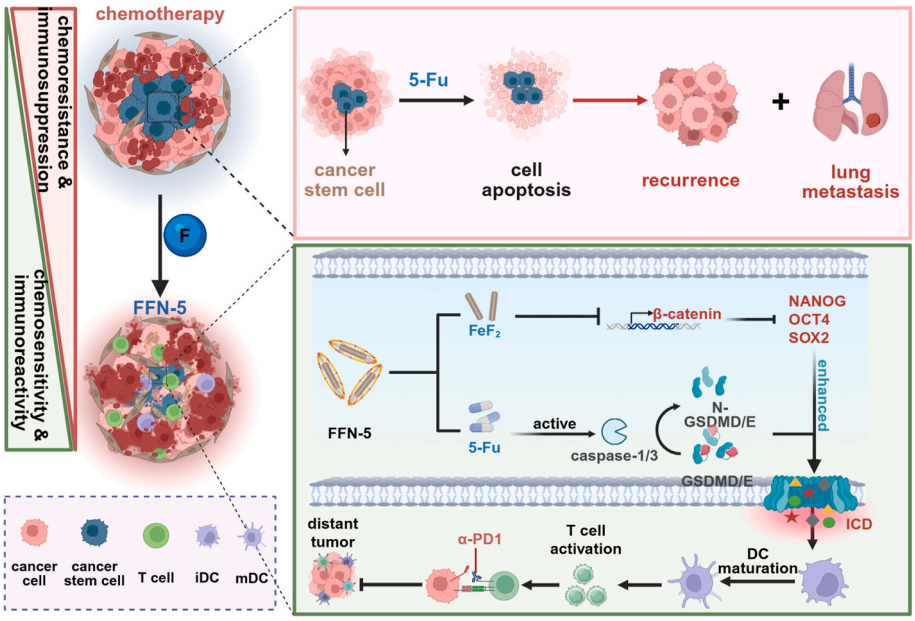

Scheme 1. Schematic diagram of FFN-5 reverse therapeutic resistance via stemness remodeling to trigger pyroptosis for chemoimmunotherapy. FFN-5 inhibit tumor stemness via Wnt/β-catenin signaling modulation, sensitize the cytotoxic sensitivity of 5-Fu in cancer cells, and effectively induce pyroptosis. These synergistic effects amplify antitumor immunity and suppress distant tumor growth and metastasis.

This effect is expected to disrupt the stable accumulation of β-catenin and inhibit its nuclear translocation, thereby reducing the transcription of downstream target genes [9,58]. Furthermore, F^- was partially reversed the DKK1 inhibitor-induced overexpression of β-catenin (Fig. S5). In summary, through comprehensive screening of nonmetallic ions, we demonstrated for the first time that F^- effectively suppressed the Wnt/β-catenin pathway by downregulating β-catenin expression and upregulating its endogenous inhibitor, DKK1 (Fig. 1n). This unique property makes F^- a promising candidate for overcoming tumor resistance and improving therapeutic outcomes.

2.2. F^- suppressed tumor stemness to potentiate chemosensitivity

The existence of CSCs significantly contributes to the development of resistance to chemotherapy [5]. To assess whether F^- could overcome chemoresistance by modulating tumor stemness, we implemented a combinatorial therapeutic strategy involving the combination of sodium fluoride (NaF) and conventional chemotherapy (Fig. 2a). The growth of tumors in mice that were treated with either NaF or 5-Fu alone was only marginally suppressed compared with that in the control group (Fig. 2b–d). Strikingly, the combination of NaF and 5-Fu significantly inhibited tumor progression. The weight of the tumor harvested on day 12 was consistent with this finding (Fig. 2e). Furthermore, across all the treatment groups, no substantial decrease in body weight was noted, suggesting that F^--augmented chemotherapy was well-tolerated without overt toxicity (Fig. S6). To further substantiate the therapeutic efficacy of the diverse treatments, histological analyses of the tumor tissues were conducted, including hematoxylin and eosin (H&E) staining and Ki67 immunofluorescence analysis (Fig. 2f). There was no significant alteration in the morphology of cancer cells in the NaF group, and the proliferative capacity of these cells remained unaffected, suggesting that targeting tumor stemness alone may not effectively impede tumor progression. In contrast, the NaF combined with 5-Fu group presented the most severe tumor damage and profound proliferation inhibition, whereas 5-Fu monotherapy showed only partial effects. To further confirm that the aforementioned remarkable outcomes were attributed to the impact of F on CSCs, we conducted additional analysis on the proportion of CSCs within the tumor tissues subsequent to various treatments. CD44 and CD133, well-established surface markers for colorectal CSCs, were used to identify these cells [6]. The tumors subjected to chemotherapy exhibited an increased proportion of CSCs, whereas the NaF + 5-Fu group demonstrated a significantly reduced proportion of CSCs (Fig. 2g and h). These results strongly suggested that the improved antitumor efficacy of the combined treatment resulted primarily from F^--mediated CSC inhibition, thereby attenuating tumor chemoresistance (Fig. 2i). Collectively, these findings provided initial evidence supporting the role of F^- in suppressing CSCs, laying the groundwork for further exploration of F^- as an adjuvant to enhance the effectiveness of diverse cancer therapies.

2.3. In vitro stemness suppression potentiated the therapeutic effects of the FeF_2@5-Fu

Given the emerging significance of F in ionic-immunotherapy and the well-documented therapeutic utility of Fe in tumor therapy, combined with their recognition as FDA-approved essential trace elements, we strategically engineered the FeF_2@5-Fu nanomedicine (FFN-5) to evaluate its anticancer potential. Initial characterization by transmission electron microscopy (TEM) confirmed that the synthesized FeF_2 nanoparticles possessed a homogeneous rod-like architecture, with an average longitudinal dimension of ~55.16 nm (Fig. 3a). X-ray diffraction (XRD) analysis unequivocally identified the crystalline structure of FeF_2 (Fig. 3b), with all the observed diffraction peaks exhibiting precise concordance with the reference tetragonal FeF_2 phase (JCPDS 45–1062). To achieve the optimal therapeutic outcome within a safe dosage range, we explored the synergistic cytotoxic effect of FeF_2 and 5-Fu on CT26 cells. When the concentration of FeF_2 reached 75 μg/mL and that of 5-Fu reached 100 μM, a remarkable cytotoxic effect on CT26 cells was observed (Fig. S9). Based on these findings, FFN-5 was synthesized using these concentrations. Subsequent surface modification with DSPE-PEG-NH_2 followed by electrostatic complexation with 5-Fu yielded the final FFN-5 formulation. The significant reduction in zeta potential provided compelling evidence for successful 5-Fu loading onto the nanocarrier (Fig. 3c; Fig. S7). Complementary verification through Fourier transform infrared spectroscopy (FT-IR) analysis identified distinctive vibrational modes characteristic of 5-Fu, thereby corroborating the successful fabrication of FFN-5 (Fig. 3d). The changes in particle size before and after 5-Fu modification further validated the

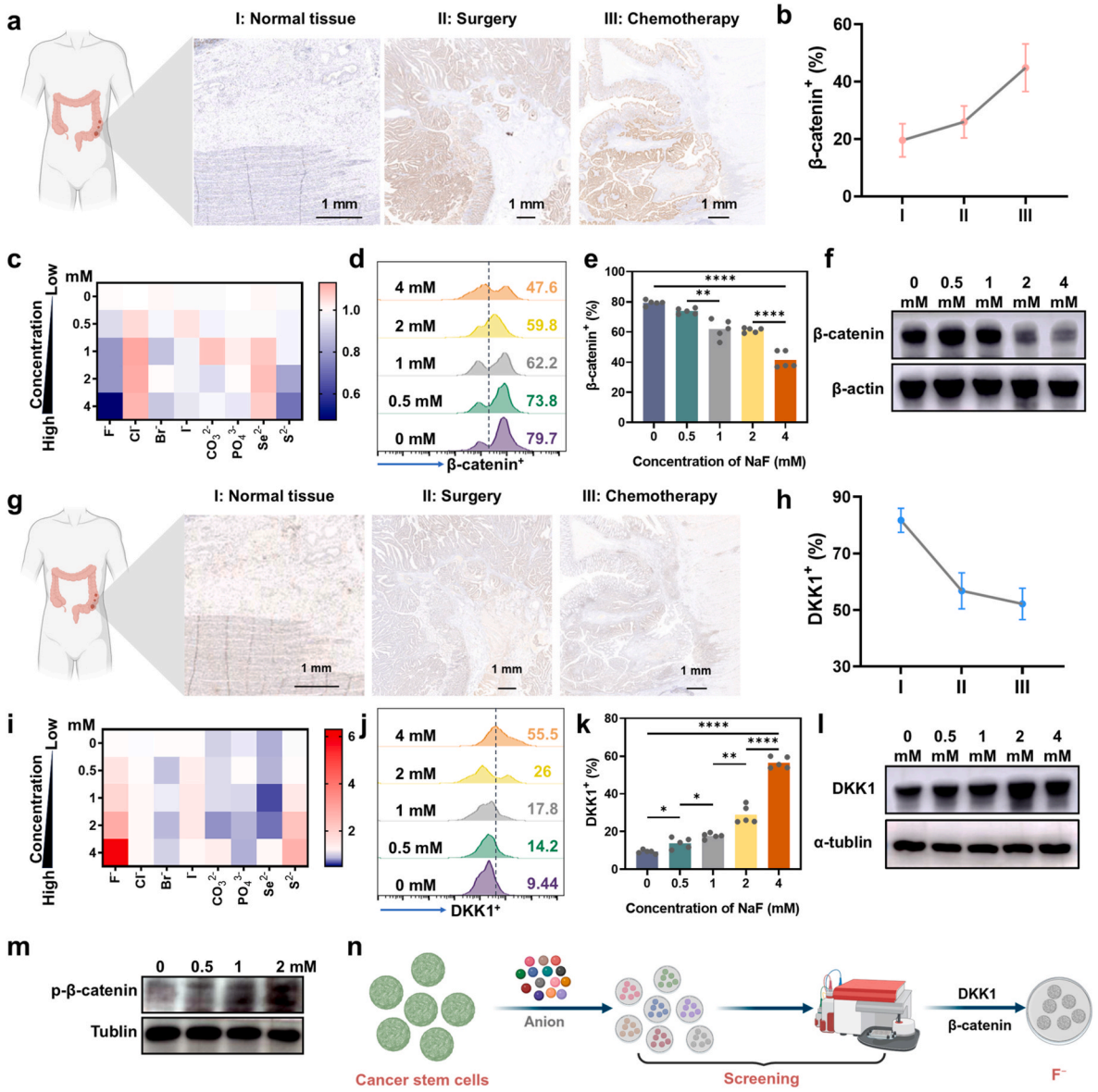

Fig. 1. Screening of nonmetallic ions for tumor stemness inhibition. (a&b) Immunohistochemical staining (a) and statistical data (b) of β-catenin in normal tissues and tumor tissues obtained from colorectal cancer patients receiving different treatments. (c) The statistical data of β-catenin expression after co-incubation of different nonmetallic ions with CT26 cells for 24 h via flow cytometry. (d&e) Representative flow cytometry (d) and statistical data (e) of the expression of β-catenin following the co-incubation of CT26 cells with different concentrations of F for 24 h. (f) Western blot analysis of β-catenin expression following the incubation of CT26 cells with various concentrations of F for a duration of 24 h. (g&h) Immunohistochemical staining (g) and statistical data (h) of DKK1 in normal tissues and tumor tissues obtained from colorectal cancer patients receiving different treatments. (i) The statistical data of DKK1 expression after co-incubation of different non-metal ions with CT26 cells for 24 h via flow cytometry. (j&k) Representative flow cytometry images (j) and statistical data (k) of the expression of DKK1 following the co-incubation of CT26 cells with different concentrations of F for 24 h. (l) Western blot analysis of DKK1 expression following the incubation of CT26 cells with various concentrations of F for a duration of 24 h. (m) Western blot analysis of p-β-catenin following the incubation of CT26 cells with various concentrations of F for a duration of 24 h. (n) Schematic diagram of ion screening. Data are shown as mean values ± SD in b, h, e, and k. n = 3 in b and h; n = 5 in e and k. Statistical significance was calculated via one-way ANOVA and is denoted as *p < 0.05, **p < 0.01, and ****p < 0.0001.

successful synthesis of FFN-5 (Fig. S8). These comprehensive physico-chemical characterizations collectively verified the successful synthesis of FFN-5 with the desired properties. To facilitate its more effective application in tumor treatment, we conducted an analysis of the stability of FFN-5 under physiological conditions. These findings indicated that FFN-5 demonstrated outstanding stability within a normal physiological environment (Fig. S10). However, under acidic conditions, 5-Fu was gradually released from FFN-5 (Fig. 3e), which can be attributed to protonation-induced structural disintegration [59,60].

The potential biological effects of the FFN-5 prompted us to further investigate its *in vitro* therapeutic efficacy against cancer cells. The monotherapeutic administration of either 5-Fu or FeF_2 nanoparticles demonstrated moderate cytotoxic effects against malignant cells, which were mechanistically attributable to conventional chemotherapy-induced apoptosis and Fe-triggered ferroptosis, respectively (Fig. 3f). Strikingly, the FFN-5 combination system manifested substantially increased tumoricidal efficacy, achieving over 80% neoplastic cell elimination. To elucidate the underlying mechanisms, we investigated changes in the mitochondrial membrane potential using JC-1 staining (Fig. 3g and h). Remarkably, CT26 cells treated with FFN-5 displayed the most intense JC-1 monomer signal, indicating profound mitochondrial membrane depolarization and concomitant oxidative stress

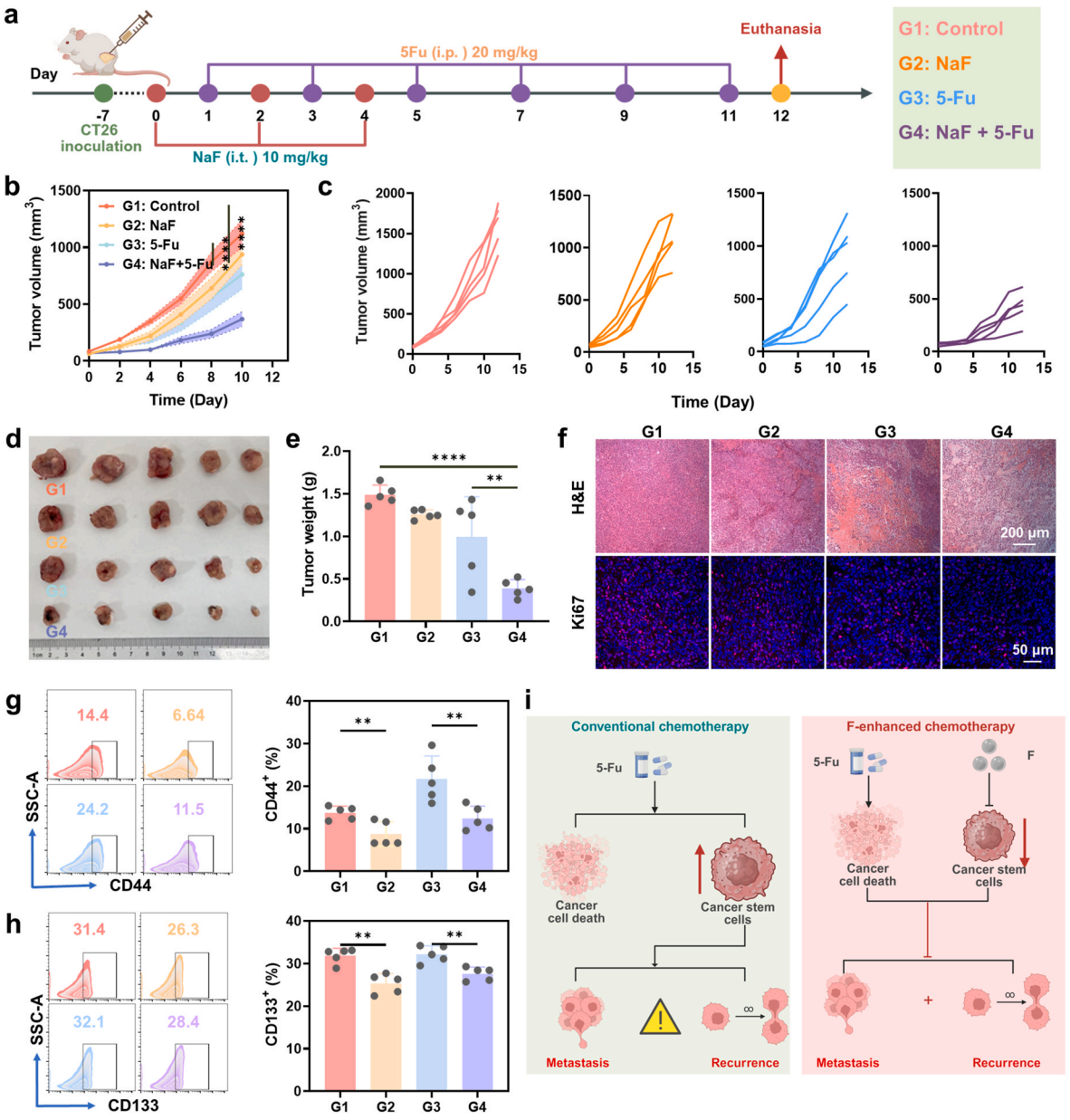

Fig. 2. F ions reduced the stemness of cancer cells and enhanced the efficacy of chemotherapy. (a) Schematic diagram showing the treatment for mice bearing the CT26 tumor. (b) The dynamic growth curves of CT26 tumors across treatment groups. (c) The individual dynamic growth curves of CT26 tumors across treatment groups. (d) The image of the CT26 tumor on the 12th day after receiving different treatments. (e) The tumor weight following exposure to different treatments. (f) H&E and Ki67 staining of tumor samples treated with different methods. (g) Flow cytometry analysis and data statistics of the proportion of $CD44^+$ cells within the tumors. (h) Flow cytometry analysis and data statistics of the proportion of $CD133^+$ cells within the tumors. (i) Schematic illustration of traditional chemotherapy and F-enhanced chemotherapy. Data are shown as mean ± SEM (b) or mean ± SD (e, g, h), unless otherwise specified. n = 5 in b, e, g, and h. Statistical significance was calculated via one-way ANOVA and is denoted as $^{**}p < 0.01$, and $^{****}p < 0.0001$.

amplification. Recognizing the critical role of CSCs in tumor aggressiveness and treatment resistance, we specifically examined the stemness-modulatory capacity of FFN-5, particularly in light of our discoveries regarding F-mediated CSC regulation. Quantitative flow cytometric assessment revealed that FFN-5 intervention substantially attenuated β-catenin expression while reciprocally augmenting its endogenous inhibitor DKK1 (Fig. 3i–l). In contrast, 5-Fu monotherapy paradoxically suppressed DKK1 expression, thereby activating the pro-survival Wnt/β-catenin pathway and potentially contributing to chemoresistance. Furthermore, the impact of FFN-5 on the characteristics of stem-like spheres was investigated by subjecting CT26 tumor spheres to various treatments. Given the established roles of SOX2, OCT4, and NANOG as master transcriptional regulators governing CSC maintenance and self-renewal [5,9], we quantified their expression patterns following therapeutic exposure. Comparative analysis revealed that while 5-Fu treatment elicited partial intensification of SOX2, OCT4, and NANOG fluorescent signals relative to those of the controls, FFN-5 administration provoked a significant decrease in these stemness markers (Fig. 3m–o; Fig. S11). Collectively, these comprehensive *in vitro* studies provided strong experimental evidence that our innovatively designed FFN-5 nanotherapeutic platform significantly improves sensitivity to chemotherapy by effectively suppressing cancer stemness characteristics, thereby overcoming a key limitation of conventional chemotherapy.

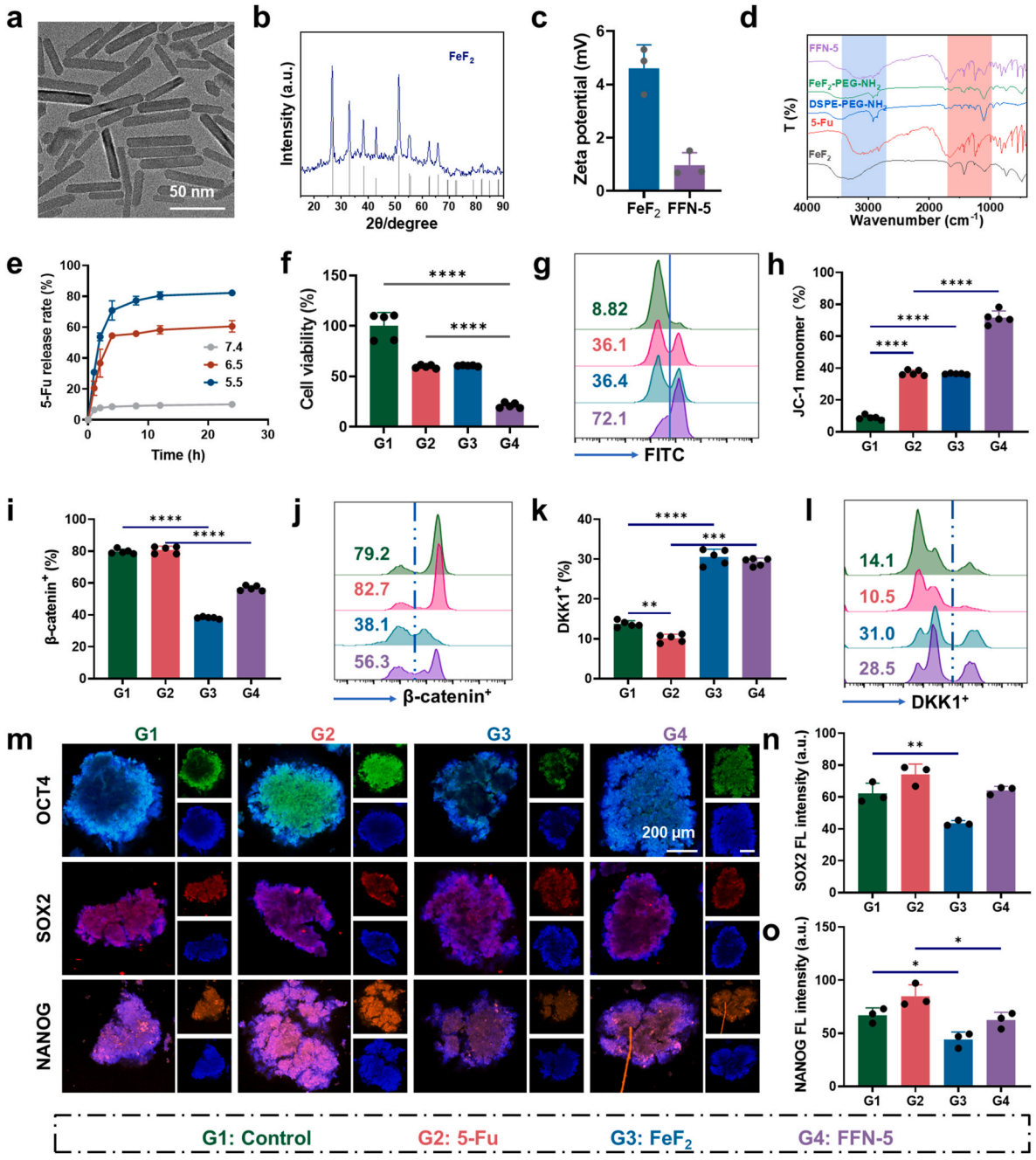

Fig. 3. FFN-5 mediated cytotoxicity and decreased stemness. (a) TEM image of FeF_2. (b) XRD pattern acquired from the as-synthesized FeF_2. (c) Zeta potential of FeF_2 and FFN-5. (d) FT-IR spectra of FeF_2, 5-Fu, DSPE-PEG-NH_2, FeF_2-PEG-NH_2, and FFN-5. (e) The release profile of 5-Fu in solutions with various pH values. (f) CT26 cell viability after different treatments. (g&h) Representative flow cytometry (g) and quantitative analysis (h) of the JC-1 monomer in CT26 cells. (i&j) Representative flow cytometry (j) and quantitative analysis (i) of the β-catenin expression in CT26 cells. (k&l) Representative flow cytometry (l) and quantitative analysis (k) of the DKK1 expression in CT26 cell. (m) Confocal images showing the expression of stemness-associated genes (OCT4, SOX2, and NANOG) in CT26 tumor spheres. (n&o) Quantitative analysis of the fluorescence intensities of SOX2 (n) and NANOG (o) following various treatments. Data are shown as mean values ± SD in e, g, h, j, m, and n. n = 5 in e, g, h, and j. n = 3 in m and n. Statistical significance was calculated via one-way ANOVA and is denoted as *p < 0.05, **p < 0.01, and ****p < 0.0001.

2.4. In vitro anti-tumor effects of FFN-5 through stemness inhibition and pyroptosis induction

Effective inhibition of tumor cell stemness renders tumor cells more susceptible to therapeutic interventions, thereby activating key signaling pathways and promoting cell death [15,40]. Following FFN-5 administration, CT26 cells displayed pronounced cellular swelling, a pathognomonic morphological hallmark of pyroptosis (Fig. 4a), in stark contrast to the limited pyroptosis observed in both the 5-Fu and the FeF_2 monotherapy groups. The molecular execution of pyroptosis is principally mediated through gasdermin (GSDM) family proteins, which undergo caspase-mediated proteolytic cleavage to yield N-terminal fragments that oligomerize to form plasma membrane pores, thereby instigating inflammatory cell death. WB analysis of GSDM-related proteins revealed that FFN-5 treatment specifically promoted the activation of cleaved caspase-1/3 (CC1/3) and the generation of N-GSDMD/N-GSDME fragments (Fig. 4b and c). These findings collectively suggested that FFN-5 substantially augmented the tumoricidal

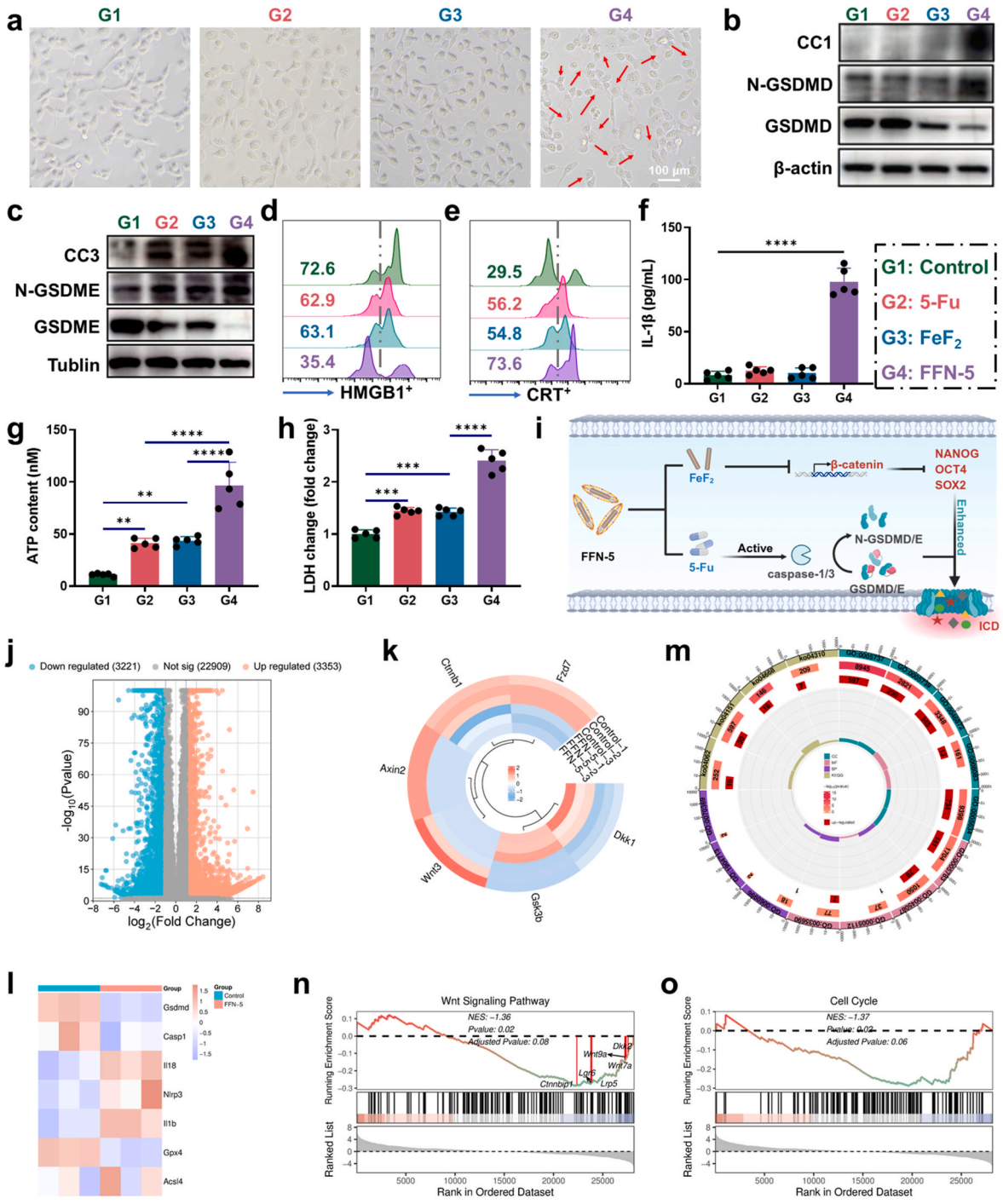

Fig. 4. FFN-5 triggered pyroptosis in CT26 cells and mediated ICD. (a) The morphological changes of CT26 cells following various treatments. (b&c) Western blot analysis of the changes in proteins related to the GSDMD and GSDME pathways. (d) Flow cytometry analysis of HMGB1 release. (e) Flow cytometry analysis of CRT expression. (f–h) The release contents of IL-1β (f), ATP (g), and LDH (h). (i) Schematic diagram of pyroptosis triggered by FFN-5. (j) Volcano plot of differentially expressed genes between control and FFN-5. (k) Circular heat map of differentially expressed genes related to the Wnt/β-catenin pathway between the control and FFN-5 groups. (l) Heat map of differentially expressed genes related to the pyroptosis and ferroptosis between the control and FFN-5 groups. (m) Gene ontology (GO) analysis on the pathways enriched with differentially expressed genes. (n&o) Gene set enrichment analysis (GSEA) of Wnt/β-catenin (n) and cell cycle (o). Data are shown as mean ± SD. n = 5 in f, g, and h. Statistical significance was calculated via one-way ANOVA and is denoted as $^{**}p < 0.01$, $^{***}p < 0.001$ and $^{****}p < 0.0001$.

activity of 5-Fu through a dual mechanism involving stemness attenuation and concomitant pyroptosis induction. Furthermore, pyroptosis elicits potent immune responses by releasing damage-associated molecular patterns (DAMPs) [29]. The hallmarks of ICD include the cell surface exposure of calreticulin (CRT), the extracellular release of interleukin-1β (IL-1β) and adenosine triphosphate (ATP), the liberation of high mobility group box 1 (HMGB1) from the nucleus, and the efflux of lactate dehydrogenase (LDH). The results revealed CRT translocation to CT26 cell plasma membranes and HMGB1 release from the nuclei in both the 5-Fu and the FeF_2 treatment groups, with the most substantial effects observed in the FFN-5 group (Fig. 4d and e; Figs. S12 and S13), confirming that FFN-5-mediated pyroptosis effectively induces ICD. In addition, quantitative assessment of IL-1β, LDH, and ATP release further corroborated these observations, with CT26 cells treated with FFN-5

exhibiting maximal extracellular concentrations of both DAMPs (Fig. 4f–h). Thus, the mechanistic sequence of FFN-5-induced pyroptosis can be summarized as follows (Fig. 4i): upon cellular internalization, the FeF_2 component effectively suppresses cancer stemness properties via β-catenin pathway inhibition, thereby circumventing conventional chemoresistance mechanisms. This stemness modulation enables 5-Fu to robustly activate the caspase/GSDM pyroptotic axis, culminating in extensive DAMP release and potent ICD initiation.

The dual capacity of FFN-5 to regulate tumor stemness and exert cytotoxic effects prompted further investigation into its underlying mechanisms. Accordingly, we performed transcriptome analysis to identify changes in mRNA expression in FFN-5-treated CT26 cells. Substantial differences in the transcriptome were observed between the treatment group and the control group. Compared with the control group, the FFN-5 group exhibited 3353 up-regulated genes and 3221 down-regulated genes (Fig. 4j). Heatmaps revealed a marked difference in stemness-associated gene expression across treatment groups (Fig. 4k). Specifically, there was a notable change in genes associated with the Wnt pathways. For example, Wnt3, Fzd7, Axin2, and Ctnnb1 were downregulated, and Gsk3b and DKK1 were upregulated in the FFN-5 group. Furthermore, compared with the control group, the FFN-5 group exhibited significant alterations in genes associated with pyroptosis, such as the upregulation of Nlrp3, Il1b, and Il18, and the downregulation of Gsdmd and Casp1 (Fig. 4l). Furthermore, FFN-5 treatment

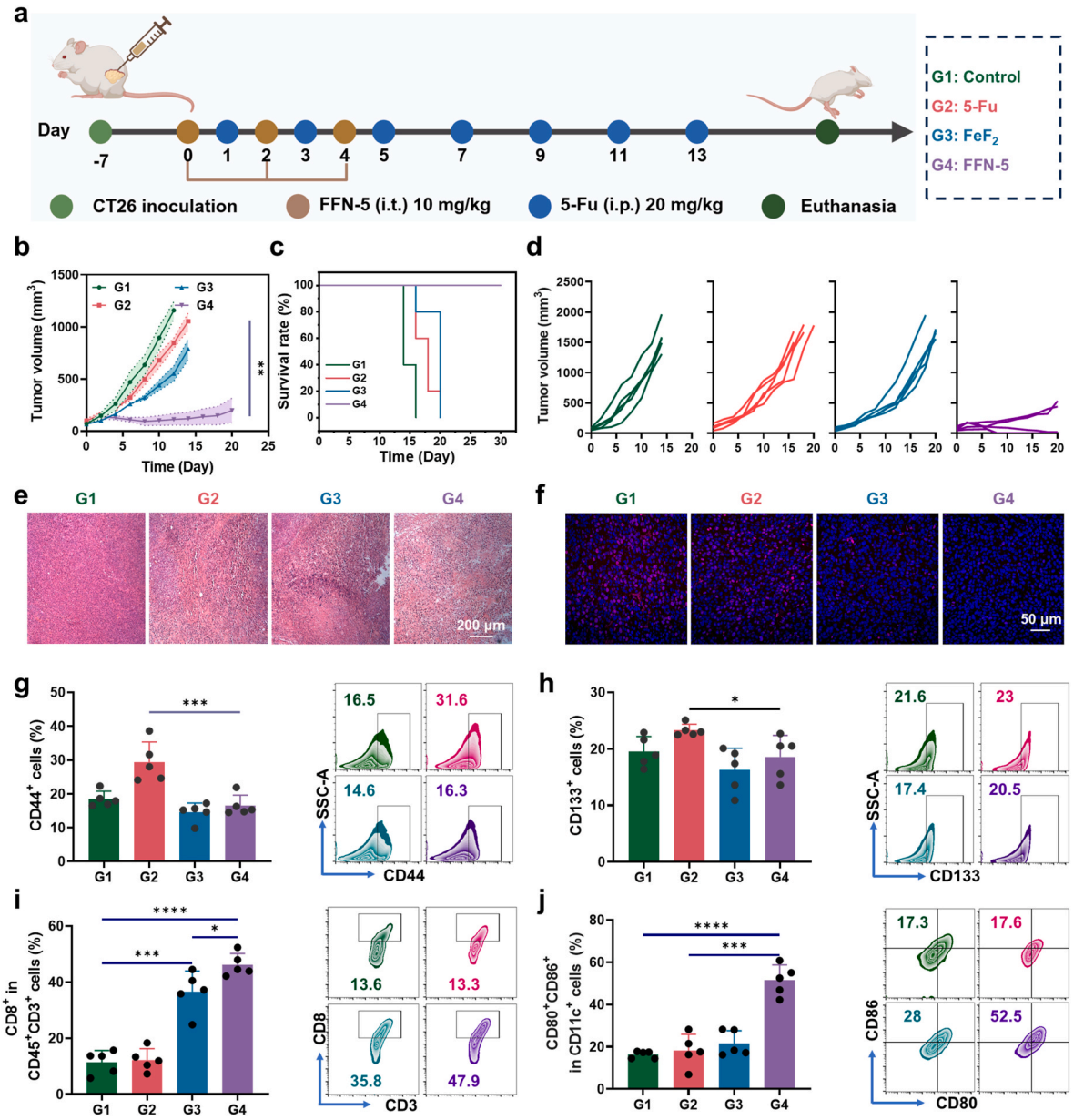

Fig. 5. Antitumor effects of FFN-5 and TME remodeling in vivo. (a) Schematic illustration of the FFN-5 treatment protocol. (b) The dynamic growth curves of CT26 tumors following various treatments. (c) The survival curves of mice after receiving various treatments. (d) The individual dynamic growth curves of CT26 tumors. (e&f) H&E (e) and Ki67 (f) staining of tumor sections. (g) Representative flow cytometry plots and corresponding quantification of the proportion of $CD44^+$ cells within tumors following various treatments. (h) Representative flow cytometry plots and corresponding quantification of the proportion of $CD133^+$ cells within tumors following various treatments. (i) Representative flow cytometry plots and corresponding quantification of the proportion of $CD8^+$ in $CD3^+CD45^+$ cells within tumors following various treatments. (j) Representative flow cytometry plots and corresponding quantification of the proportion of $CD80^+CD86^+$ in $CD11c^+$ cells within tumors following various treatments. Data are shown as mean ± SEM in b. Data are shown as mean ± SD in g-j. n = 5 in b, c, g-j. Statistical significance was calculated via one-way ANOVA and is denoted as *p < 0.05, **p < 0.01, ***p < 0.001, and ****p < 0.0001.

resulted in altered expression of Gpx4 and Acsl4, suggesting that it could also induce ferroptosis. However, the alterations in ferroptosis-related genes were less pronounced than those associated with pyroptosis, indicating that pyroptosis represents the predominant form of cell death induced by FFN-5 in CT26 cells. To elucidate the functions of those differentially expressed genes whose expression was high, a Gene Ontology (GO) analysis was carried out. The TNF signaling pathway within the cell, the innate immune response, and the chemokine signaling pathway were significantly upregulated (Fig. 4m). These findings indicated that FFN-5 treatment triggered the immune response of cancer cells. Gene set enrichment analysis (GSEA) was employed to assess the enrichment situation of the entire gene set. Among the significantly changed signaling pathways, the Wnt/β-catenin signaling pathway (Fig. 4n) and the cell cycle (Fig. 4o) were significantly downregulated, indicating that FFN-5 treatment inhibited cell division and proliferation. These omics-level findings provided compelling molecular evidence that FFN-5 orchestrates its anti-tumor effects through coordinated inhibition of Wnt/β-catenin-mediated stemness and potent activation of inflammatory pyroptosis.

2.5. *In vivo antitumor therapy and immune response evaluation*

Building upon the remarkable *in vitro* antitumor activity of FFN-5 in stemness inhibition-mediated pyroptosis induction and immune activation, we systematically evaluated its therapeutic potential in a CT26 tumor-bearing mouse model (Fig. 5a). The study included four randomized treatment cohorts (n = 5 each): G1: control, G2: 5-Fu, G3: FeF_2, and G4: FFN-5. Tumor growth kinetics, monitored through caliper measurements every other day, revealed distinct therapeutic responses across treatment groups. Compared with the more aggressive growth of CT26 tumors observed in the control group, 5-Fu or FeF_2 treatment slightly inhibited tumor growth (Fig. 5b–d). Strikingly, the FFN-5 treatment demonstrated the most pronounced inhibitory effect on tumor growth, which was attributable to the synergistic interplay between cancer stem cell suppression and enhanced 5-Fu-mediated tumor cell eradication. Importantly, FFN-5 treatment conferred a significant survival advantage, with ~100 % of the treated mice surviving beyond the 30-day experimental endpoint (Fig. 5c). Moreover, comprehensive histopathological evaluation through H&E staining and Ki67 immunofluorescence analysis provided further validation of therapeutic efficacy (Fig. 5e and f). After treatment with FFN-5, the cancer cells exhibited severe nuclear contraction and rupture, accompanied by significant down-regulation of the expression of Ki67 (Fig. S14), a marker of cell proliferation. These findings collectively substantiated the superior antitumor performance of FFN-5 in vivo. In addition, serum biochemical and hematological parameters were measured in mice injected with FFN-5 over a 15-day period (Figs. S15 and S16). All values remained within normal ranges, indicating no significant signs of systemic toxicity.

To elucidate the mechanistic basis of the enhanced therapeutic efficacy of FFN-5, we conducted a systematic analysis of cancer stemness modulation and immune microenvironment remodeling. The proportion of CSCs in tumors was assessed by examining the expression levels of the CD44 and CD133 markers following various treatments (Fig. 5g and h). FeF_2 partially reduced the proportion of $CD44^+$ and $CD133^+$ cells, whereas 5-Fu markedly increased this proportion, suggesting that chemotherapy may induce drug resistance in tumor cells. Notably, FFN-5 significantly decreased the proportion of $CD44^+$ and $CD133^+$ cells compared with 5-Fu treatment alone, indicating its potential to enhance cellular sensitivity to 5-Fu-induced cytotoxicity. As crucial components of the immune system, $CD8^+$ T cells recognize tumor-specific antigens and eliminate cancer cells through the secretion of perforin and granzymes. The analysis of T-cell infiltration in tumor tissues revealed that the FFN-5 treatment group presented a greater proportion (~47.9 %) of $CD8^+$ cells within the $CD45^+CD3^+$ T cell population than both the 5-Fu group (~13.3 %) and the FeF_2 group (~35.8 %), suggesting effective activation of the antitumor immune system (Fig. 5i). Moreover, there was a substantial increase in the proportion of dendritic cells (DCs) within the FFN-5 groups (Fig. 5j). These results indicated that FFN-5-induced inhibition of CSCs and the subsequent significant activation of pyroptosis in tumor cells effectively enhanced the immune response. This led to DC maturation and increased T-cell infiltration, thereby shifting the TME from immune suppression to immune activation, which ultimately facilitated the effective elimination of tumor tissues.

2.6. *Chemoimmunotherapy via FFN-5 inhibited distal tumors and metastases*

The field of cancer treatment has been revolutionized by immunotherapy, particularly ICB therapy; however, its clinical efficacy is curtailed by tumor heterogeneity and immune evasion [17,61]. Given that FFN-5-induced pyroptosis creates an inflammatory immune microenvironment, we hypothesized that combining FFN-5 with ICB could enhance systemic antitumor responses. To evaluate this, we established a bilateral tumor model with four experimental groups: the control group (G1), α-PD1 group (G2), FFN-5 group (G3), and the FFN-5 plus α-PD1 combination group (G4) (Fig. 6a). The administration of the α-PD1 antibody resulted in slight inhibition of both primary and distant tumors, potentially due to the rapid clearance of antibodies and insufficient activation of the immune response (Fig. 6b–e). In contrast to the control and α-PD1 groups, the FFN-5 group not only impeded the growth of the primary tumor but also significantly restricted the proliferation of the distant tumor. The combination of FFN-5 and α-PD1 demonstrated the anticipated efficacy, resulting in the most favorable therapeutic outcome against both tumors (Fig. S17). Therefore, the combination approach involving FFN-5 along with α-PD1 has great potential for inhibiting the proliferation of both primary and distant tumors. Moreover, there was no notable alteration in the weight of the mice (Fig. S18). Given the established role of CSCs in metastatic dissemination, we further investigated the anti-metastatic potential of FFN-5 using an experimental lung metastasis model (Fig. 6f). The tumor cells were pre-incubated with 5-Fu and further incubated with FeF_2 or NaF for 24 h before being intravenously injected into the mice. The results revealed a moderate decrease in lung weight in the mice treated with NaF, whereas the mice treated with FeF_2 exhibited a significant decrease in lung weight and a notable increase in survival time (Fig. 6h and i). Additionally, the results of lung immunohistochemical staining revealed that untreated mice exhibited severe lung metastasis, which was mitigated following NaF treatment (Fig. 6g–j; Fig. S19). Conversely, the FeF_2 treatment group presented the lowest number of tumor metastases in the mice, highlighting the potential advantages of FFN-5 as an innovative nanomedicine. These findings underscored the potential of FFN-5 as a multifaceted nanotherapeutic platform capable of simultaneously addressing primary tumors, distant lesions, and metastatic spread.

3. Conclusion

In summary, we developed a novel strategy leveraging metal fluoride-based modulation of Wnt/β-catenin signaling to simultaneously overcome treatment resistance and activate pyroptosis-mediated immune responses. Our systematic screening identified F^- as potent inhibitors of β-catenin-driven tumor stemness, establishing a foundation for enhanced chemoimmunotherapy. The engineered FFN-5 demonstrated remarkable therapeutic potential by effectively suppressing cancer stemness, enhancing 5-Fu cytotoxicity, and inducing immunogenic pyroptosis. In addition to local tumor control, FFN-5 treatment reshaped the immunosuppressive TME, promoting DC maturation and cytotoxic T cell infiltration. When combined with ICB, this approach elicited robust systemic antitumor immunity, achieving significant suppression of both primary and distal lesions. Moreover, the unique stemness-regulating capability of F-based nanomodulators conferred pronounced antimetastatic effects, further highlighting the versatility of

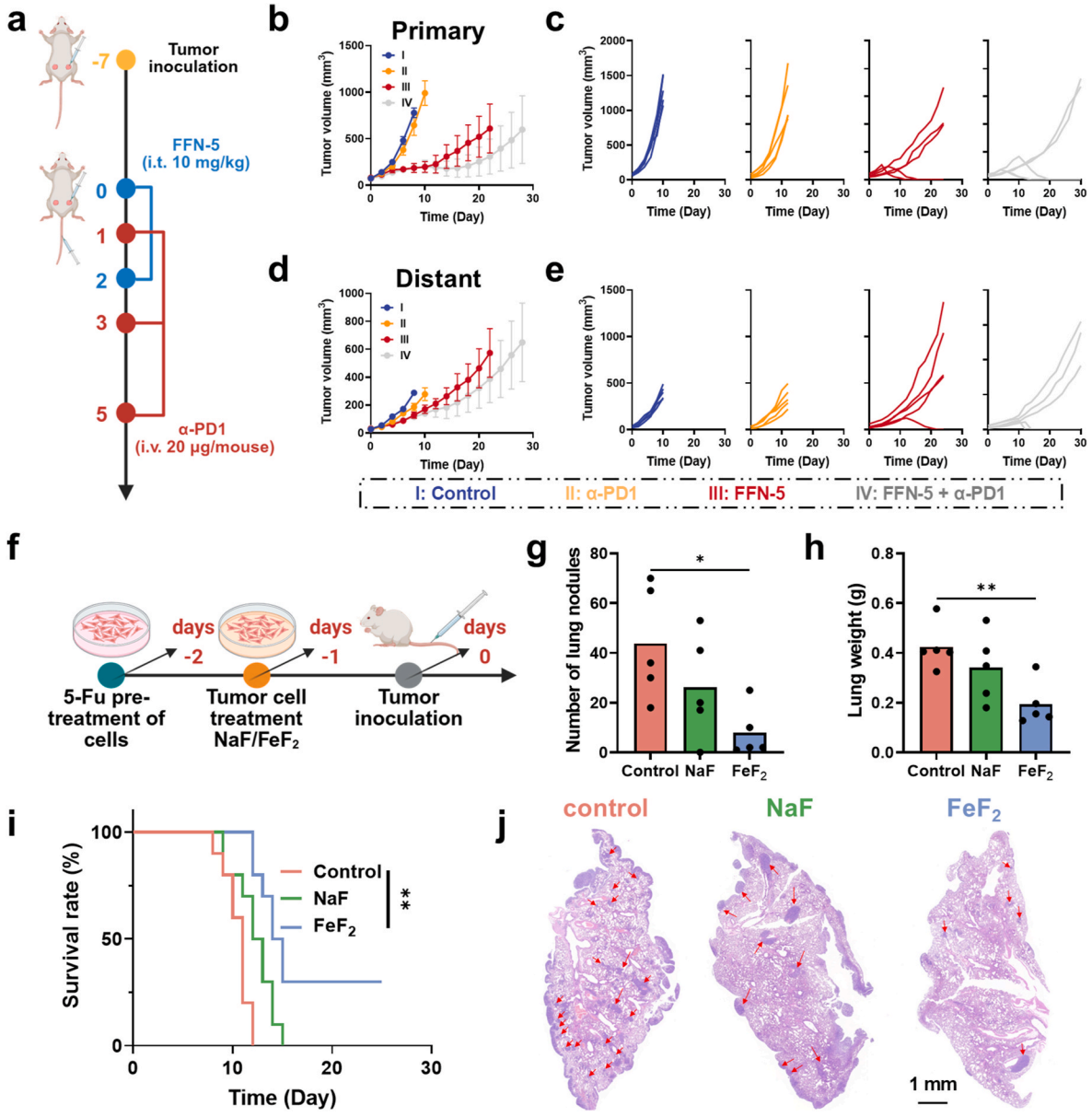

Fig. 6. FFN-5 improved the efficacy of ICB treatment and suppressed the development of lung metastasis. (a) Schematic diagram of the combination of FFN-5 and ICB treatment for CT26 tumors. (b) The dynamic growth curves of the primary tumors following various treatments. (c) The dynamic individual growth curves of the primary tumors across treatment groups. (d) The dynamic growth curves of the distant tumors following various treatments. (e) The dynamic individual growth curves of the distant tumors across treatment groups. (f) Schematic diagram of FFN-5 treatment for lung metastasis of CT26 tumors. (g) Statistics on the number of lung nodules in mice seven days after different treatments. (h) The lung weights seven days after different treatments. (i) Survival curves of mice with lung metastases after different treatments. (j) Representative H&E staining images of the lungs seven days following various treatments. Data are shown as mean ± SEM in b and d. n = 5 in b, d, g, and h. n = 10 in i. Statistical significance was calculated via one-way ANOVA and is denoted as *p < 0.05 and **p < 0.01.

this strategy. Our work not only elucidated the critical role of F^- in modulating cancer stemness but also presented FFN-5 as a multifunctional nanoplatform that synergizes with chemotherapy and immunotherapy through stemness-dependent mechanisms. By addressing the dual challenges of chemoresistance and immune evasion, our findings offer a promising translational framework for overcoming treatment limitations. Future studies exploring optimized dosing regimens and broader combination therapies will further advance this innovative approach toward clinical application.

CRediT authorship contribution statement

Shumin Sun: Writing – original draft, Formal analysis, Data curation. **Nailin Yang:** Writing – review & editing, Project administration. **Jihu Nie:** Formal analysis, Data curation. **Linzhu Zhang:** Formal analysis, Data curation. **Di Wang:** Formal analysis, Data curation. **Xingwei Sun:** Formal analysis, Data curation. **Yong Jin:** Resources. **Liang Cheng:** Writing – review & editing, Supervision, Project administration.

Ethics approval and consent to participate

Ethics Committee of Soochow University has approved the animal experiments (202406A0726).

Declaration of competing interest

The authors declare that they have no known competing financial interests or personal relationships that could have appeared to influence

the work reported in this paper.

Acknowledgements

This article was partially supported by the National Research Programs of China (2022YFB3804600), National Natural Science Foundation of China (52472288, 52403386), Collaborative Innovation Center of Suzhou Nano Science and Technology, the 111 Project, and Joint International Research Laboratory of Carbon-Based Functional Materials and Devices, Medical Research Project of Jiangsu Province (ZD2022024), Science and Technology Development Fund, Macau SAR (0118/2023/RIA2, 0064/2024/AMJ, 0016/2024/RIA1), the Research project of China Baoyuan Investment Co., Ltd. N.Y. was supported by the Macao Young Scholars Program and the Jiangsu Funding Program for Excellent Postdoctoral Talent.

Appendix A. Supplementary data

Supplementary data to this article can be found online at https://doi.org/10.1016/j.bioactmat.2025.10.011.

References

[1] R.L. Siegel, A.N. Giaquinto, A. Jemal, Cancer statistics, CA-Cancer J. Clin. 74 (1) (2024) 12–49, 2024.
[2] Y. Xi, P. Xu, Global colorectal cancer burden in 2020 and projections to 2040, Transl, Oncol 14 (10) (2021) 101174.
[3] R.A. Ward, S. Fawell, N. Floc'h, V. Flemington, D. McKerrecher, P.D. Smith, Challenges and opportunities in cancer drug resistance, Chem. Rev. 121 (6) (2020) 3297–3351.
[4] M. Russo, M. Chen, E. Mariella, H. Peng, S.K. Rehman, E. Sancho, A. Sogari, T. S. Toh, N.Q. Balaban, E. Batlle, Cancer drug-tolerant persister cells: from biological questions to clinical opportunities, Nat. Rev. Cancer 24 (10) (2024) 694–717.
[5] X. Chu, W. Tian, J. Ning, G. Xiao, Y. Zhou, Z. Wang, Z. Zhai, G. Tanzhu, J. Yang, R. Zhou, Cancer stem cells: advances in knowledge and implications for cancer therapy, Signal Transduct. Target. Ther. 9 (1) (2024) 170.
[6] Y. Liu, H. Wang, Biomarkers and targeted therapy for cancer stem cells, Trends Pharmacol. Sci. 45 (1) (2024) 56–66.
[7] Z. Li, J. Yang, B. Ren, Q. Fan, L. Huang, S. Guo, R. Zhou, S. Chen, J. Feng, C. Yan, Double-Layered hollow mesoporous cuprous oxide nanoparticles for double drug sequential therapy of tumors, Adv. Mater. 36 (28) (2024) 2313212.
[8] Q. Deng, A. Hua, Q. Zhao, Z. Zhang, T. Yang, Q. Wang, X. Yang, Z. Li, Modulating tumor acidity with hydroxyethyl starch-based nanoparticles by targeting CA9 to eliminate cancer stem cells and overcome immunosuppression, Biomaterials 324 (2025) 123501.
[9] S. Sun, N. Yang, Z. Pei, F. Gong, L. Cheng, Biomedical engineering targeting cancer stem cells to reinforce cancer therapy, Coord. Chem. Rev. 530 (2025) 216494.
[10] L. Zhang, S. Sun, D. Wang, N. Yang, D. Wang, J. Nie, Z. Pei, J. Qin, L. Zhang, H. Zhu, Lactate-Modulating nanoreactors facilitate self-amplifying pyroptosis and the cGAS-STING Cascade for potentiated catalytic-immunotherapy, Adv. Sci. (2025) e11144.
[11] P. Song, Z. Gao, Y. Bao, L. Chen, Y. Huang, Y. Liu, Q. Dong, X. Wei, Wnt/β-catenin signaling pathway in carcinogenesis and cancer therapy, J. Hematol. Oncol. 17 (1) (2024) 46.
[12] H. Tanton, T. Sewastianik, H.-S. Seo, D. Remillard, R.S. Pierre, P. Bala, D. Aitymbayev, P. Dennis, K. Adler, E. Geffken, A novel β-catenin/BCL9 complex inhibitor blocks oncogenic wnt signaling and disrupts cholesterol homeostasis in colorectal cancer, Sci. Adv. 8 (17) (2022) eabm3108.
[13] F.A. Gowans, N. Forte, J. Hatcher, O.W. Huang, Y. Wang, B.E. Altamirano Poblano, I.E. Wertz, D.K. Nomura, Covalent degrader of the oncogenic transcription factor β-Catenin, J. Am. Chem. Soc. 146 (24) (2024) 16856–16865.
[14] Y. Xu, Y. Yu, R. Yan, X. Ke, Y. Qu, Modulating β-catenin homeostasis for cancer therapy, Trends Cancer 10 (6) (2024) 507–518.
[15] S. Shen, X. Xu, S. Lin, Y. Zhang, H. Liu, C. Zhang, R. Mo, A nanotherapeutic strategy to overcome chemotherapeutic resistance of cancer stem-like cells, Nat. Nanotechnol. 16 (1) (2021) 104–113.
[16] Q. Wang, H. Cao, X. Hou, D. Wang, Z. Wang, Y. Shang, S. Zhang, J. Liu, C. Ren, J. Liu, Cancer stem-like cells-oriented surface self-assembly to conquer radioresistance, Adv. Mater. 35 (38) (2023) 2302916.
[17] F.G. Dall'Olio, A. Marabelle, C. Caramella, C. Garcia, M. Aldea, N. Chaput, C. Robert, B. Besse, Tumour burden and efficacy of immune-checkpoint inhibitors, Nat. Rev. Clin. Oncol. 19 (2) (2022) 75–90.
[18] G. Morad, B.A. Helmink, P. Sharma, J.A. Wargo, Hallmarks of response, resistance, and toxicity to immune checkpoint blockade, Cell 184 (21) (2021) 5309–5337.
[19] N. Yang, X. Sun, Y. Zhou, X. Yang, J. You, Z. Yu, J. Ge, F. Gong, Z. Xiao, Y. Jin, Liquid metal microspheres with an eddy-thermal effect for magnetic hyperthermia-enhanced cancer embolization-immunotherapy, Sci. Bull. 68 (16) (2023) 1772–1783.
[20] J.n. Zeng, Y. Jin, Y. Ao, W. Li, K. Liang, H. Chen, Y. Long, Y. Du, Modulating immune responses for enhanced cell therapies: the dual role of multi-scale biomaterials, EngMedicine 1 (3) (2024) 100038.
[21] S. Sun, N. Yang, J. Nie, Z. Yang, Z. Pei, R. Ding, L. Cheng, Nanomaterials intervene in cell senescence to reinforce cancer therapy, Coord. Chem. Rev. 545 (2025) 217012.
[22] K. Zhao, Y. Yan, X.-K. Jin, T. Pan, S.-M. Zhang, C.-H. Yang, Z.-Y. Rao, X.-Z. Zhang, An orally administered gene editing nanoparticle boosts chemo-immunotherapy in colorectal cancer, Nat. Nanotechnol. 20 (2025) 935–946.
[23] Y. Li, Y. Wu, Z. Fang, Y. Zhang, H. Ding, L. Ren, L. Zhang, Q. Gong, Z. Gu, K. Luo, Dendritic nanomedicine with boronate bonds for augmented chemo-immunotherapy via synergistic modulation of tumor immune microenvironment, Adv. Mater. 36 (2) (2024) 2307263.
[24] S. Wang, L. Liu, L. Tian, P. Xu, S. Li, L. Hu, Y. Xia, Y. Ding, J. Wang, S. Li, Elucidation of spatial cooperativity in chemo-immunotherapy by a sequential dual-ph-responsive drug delivery System, Adv. Mater. 36 (26) (2024) 2403296.
[25] Y. Zhang, H. Chen, H. Mo, N. Zhao, X. Sun, B. Liu, R. Gao, B. Xu, Z. Zhang, Z. Liu, Distinct cellular mechanisms underlie chemotherapies and PD-L1 blockade combinations in triple-negative breast cancer, Cancer Cell 43 (3) (2025) 446–463.
[26] J. Cong, P. Liu, Z. Han, W. Ying, C. Li, Y. Yang, S. Wang, J. Yang, F. Cao, J. Shen, Bile acids modified by the intestinal microbiota promote colorectal cancer growth by suppressing CD8+ T cell effector functions, Immunity 57 (4) (2024) 876–889.
[27] A. Letai, H. de The, Conventional chemotherapy: millions of cures, unresolved therapeutic index, Nat. Rev. Cancer 25 (2025) 209–218.
[28] Y.-T. Zhong, Z.-W. Qiu, K.-Y. Zhang, Z.-M. Lu, Z.-F. Li, J.-M. Nie, Y. Cen, H. Cheng, S.-Y. Li, X. Chen, Chemotherapeutics-enabled apoptosis-pyroptosis switch to trigger adaptive and innate immunity for metastatic breast cancer immunotherapy, Mater. Today 83 (2025) 263–283.
[29] Y. Liu, R. Pan, Y. Ouyang, W. Gu, T. Xiao, H. Yang, L. Tang, H. Wang, B. Xiang, P. Chen, Pyroptosis in health and disease: mechanisms, regulation and clinical perspective, Signal Transduct. Target. Ther. 9 (1) (2024) 245.
[30] J. Wu, H. Wang, P. Gao, S. Ouyang, Pyroptosis: induction and inhibition strategies for immunotherapy of diseases, Acta Pharm. Sin. B 14 (10) (2024) 4195–4227.
[31] M.J. Zhang, Y.Y. Wang, L.L. Han, X.Y. Liu, Y.Y. Xie, Z. Xu, Z.J. Sun, Biomaterials elicit pyroptosis enhancing cancer immunotherapy, Adv. Funct. Mater. 34 (7) (2024) 2311362.
[32] D. Wang, L. Zhang, J. Nie, N. Yang, S. Sun, C. Wang, Z. Pei, F. Gong, X. Sun, Y. Jin, Engineered nano-micro pyroptosis generators: a magnetic-metallo-immunotherapeutic strategy to reinforce transarterial embolization, J. Am. Chem. Soc. 147 (29) (2025) 25536–25552.
[33] L. Zhang, D. Wang, Y. Liu, N. Yang, S. Sun, C. Wang, D. Wang, J. Nie, J. Qin, L. Zhang, Metabolic modulation-driven self-reinforcing pyroptosis-STING nanoadjuvant for potentiated metalloimmunotherapy, Bioact. Mater. 53 (2025) 641–655.
[34] S. Sun, X. Huang, N. Yang, H. Lei, Z. Pei, Z. Han, L. Liu, F. Gong, Q. Yu, J. Li, Fluorinated Titanium oxide (TiO2–x F x) nanospindles as ultrasound-triggered pyroptosis inducers to boost sonodynamic immunotherapy, ACS Nano 18 (30) (2024) 19756–19770.
[35] W.-D. Wang, Z.-J. Sun, Evoking pyroptosis with nanomaterials for cancer immunotherapy: current boom and novel outlook, Nano TransMed 1 (1) (2022) e9130001.
[36] Q. Feng, F. Qi, W. Fang, P. Hu, J. Shi, Ferroptosis to pyroptosis regulation by iron-based nanocatalysts for enhanced tumor immunotherapy, J. Am. Chem. Soc. 146 (47) (2024) 32403–32414.
[37] M. Li, J. Kim, H. Rha, S. Son, M.S. Levine, Y. Xu, J.L. Sessler, J.S. Kim, Photon-controlled pyroptosis activation (photopyro): an emerging trigger for antitumor immune response, J. Am. Chem. Soc. 145 (11) (2023) 6007–6023.
[38] Z. Li, Y. Wang, F. Mo, T. Wolter, R. Hong, A. Barrett, N. Richmond, F. Liu, Y. Chen, X. Yang, Engineering pyroptotic vesicles as personalized cancer vaccines, Nat. Nanotechnol. 20 (2025) 1108–1118.
[39] Y.-T. Liu, L. Chen, S.-J. Li, W.-Y. Wang, Y.-Y. Wang, Q.-C. Yang, A. Song, M.-J. Zhang, W.-T. Mo, H. Li, Dysregulated Wnt/β-catenin signaling confers resistance to cuproptosis in cancer cells, Cell Death Differ. 31 (11) (2024) 1452–1466.
[40] H. Zheng, J. Liu, Q. Cheng, Q. Zhang, Y. Zhang, L. Jiang, Y. Huang, W. Li, Y. Zhao, G. Chen, Targeted activation of ferroptosis in colorectal cancer via LGR4 targeting overcomes acquired drug resistance, Nat. Cancer 5 (4) (2024) 572–589.
[41] S. Sun, N. Yang, J. Nie, Z. Pei, C. Wang, Z. Yang, Z. Han, Y. Cai, L. Cheng, Ferrous fluoride nanoinitiators reprogram tumor stemness to empower ultrasound-augmented pyroptosis for potent catalytic immunotherapy, Biomaterials 326 (2025) 123652.
[42] Y. Wang, C. Cao, Y. Zhu, H. Fan, Q. Liu, Y. Liu, K. Chen, Y. Wu, S. Liang, M. Li, TREM2/β-catenin attenuates NLRP3 inflammasome-mediated macrophage pyroptosis to promote bacterial clearance of pyogenic bacteria, Cell Death Dis. 13 (9) (2022) 771.
[43] X. Sun, Y. Zhang, J. Li, K.S. Park, K. Han, X. Zhou, Y. Xu, J. Nam, J. Xu, X. Shi, Amplifying STING activation by cyclic dinucleotide–manganese particles for local and systemic cancer metalloimmunotherapy, Nat. Nanotechnol. 16 (11) (2021) 1260–1270.
[44] X. Sun, X. Zhou, X. Shi, O.A. Abed, X. An, Y.L. Lei, J.J. Moon, Strategies for the development of metalloimmunotherapies, Nat. Biomed. Eng. 8 (2024) 1073–1091.
[45] Y. Luo, X. He, Q. Du, L. Xu, J. Xu, J. Wang, W. Zhang, Y. Zhong, D. Guo, Y. Liu, Metal-based smart nanosystems in cancer immunotherapy, Exploration 4 (6) (2024) 20230134.
[46] C. Scirgolea, R. Sottile, M. De Luca, A. Susana, S. Carnevale, S. Puccio, V. Ferrari, V. Lise, G. Contarini, A. Scarpa, NaCl enhances CD8+ T cell effector functions in cancer immunotherapy, Nat. Immunol. 25 (2024) 1845–1857.

[47] J. Lötscher, A.-A.M. i Líndez, N. Kirchhammer, E. Cribioli, G.M.P.G. Attianese, M. P. Trefny, M. Lenz, S.I. Rothschild, P. Strati, M. Künzli, Magnesium sensing via LFA-1 regulates CD8+ T cell effector function, Cell 185 (4) (2022) 585–602.
[48] S. Solier, S. Müller, T. Cañeque, A. Versini, A. Mansart, F. Sindikubwabo, L. Baron, L. Emam, P. Gestraud, G.D. Pantoş, A druggable copper-signalling pathway that drives inflammation, Nature 617 (7960) (2023) 386–394.
[49] S. Chen, W. Cui, Z. Chi, Q. Xiao, T. Hu, Q. Ye, K. Zhu, W. Yu, Z. Wang, C. Yu, Tumor-associated macrophages are shaped by intratumoral high potassium via Kir2. 1, Cell Metab. 34 (11) (2022) 1843–1859.
[50] N. Yang, S. Sun, J. Xu, F. Gong, H. Lei, Y. Hao, Z. Pei, C. Wang, Q. Yu, J. Nie, Manganese galvanic cells intervene in tumor metabolism to reinforce cGAS-STING activation for bidirectional synergistic hydrogen-immunotherapy, Adv. Mater. 37 (8) (2025) 2414929.
[51] Q. Yu, S. Sun, N. Yang, Z. Pei, Y. Chen, J. Nie, H. Lei, L. Wang, F. Gong, L. Cheng, Self-Cascaded Pyroptosis-STING initiators for catalytic metalloimmunotherapy, J. Am. Chem. Soc. 147 (4) (2025) 3161–3173.
[52] J. Nie, N. Yang, S. Sun, L. Wang, Z. Pei, J. Wu, Q. Yu, Z. Han, Y. Chen, L. Cheng, Antimony component schottky nanoheterojunctions as ultrasound-heightened pyroptosis initiators for sonocatalytic immunotherapy, Angew. Chem., Int. Ed. 64 (4) (2025) e202416426.
[53] X. Han, S. Sun, N. Yang, Z. Han, Z. Pei, Q. Yu, J. Nie, L. Wang, A. Liu, X. Meng, Nano-Engineered magnesium implants for magnetothermal enhanced pyroptosis to boost immunotherapy, Adv. Funct. Mater. 34 (46) (2024) 2405836.
[54] G. Hou, Y. Chen, H. Lei, Y. Lu, L. Liu, Z. Han, S. Sun, J. Li, L. Cheng, Bimetallic peroxide nanoparticles induce PANoptosis by disrupting ion homeostasis for enhanced immunotherapy, Sci. Adv. 10 (45) (2024) eadp7160.
[55] B. Ding, H. Chen, J. Tan, Q. Meng, P. Zheng, P.a. Ma, J. Lin, ZIF-8 nanoparticles evoke pyroptosis for high-efficiency cancer immunotherapy, Angew. Chem., Int. Ed. 62 (10) (2023) e202215307.
[56] G. Wang, L. Xie, B. Li, W. Sang, J. Yan, J. Li, H. Tian, W. Li, Z. Zhang, Y. Tian, A nanounit strategy reverses immune suppression of exosomal PD-L1 and is associated with enhanced ferroptosis, Nat. Commun. 12 (1) (2021) 5733.
[57] B. Liu, X. Chen, Y. Zhu, H. Chen, J. Tan, Z. Yang, J. Li, P. Zheng, L. Feng, Q. Wang, One-Step symbiosis of bimetallic peroxides nanoparticles to induce Ferroptosis/Cuproptosis and activate cGAS-STING pathway for enhanced tumor immunotherapy, Adv. Mater. 37 (21) (2025) 2500337.
[58] M.M. Maurice, S. Angers, Mechanistic insights into Wnt–β-catenin pathway activation and signal transduction, Nat. Rev. Mol. Cell Biol. 26 (5) (2025) 371–388.
[59] A.M. dos Santos, S.G. Carvalho, L.M.B. Ferreira, M. Chorilli, M.P.D. Gremião, Understanding the role of electrostatic interactions on the association of 5-fluoro-uracil to chitosan-TPP nanoparticles, Colloids Surf., A 640 (2022) 128417.
[60] A.G. Naranjo, H.V. Cobas, N.K. Gupta, K.R. Lopez, A.A. Peña, D. Sacasas, R. A. Brito, 5-Fluorouracil uptake and release from pH-responsive nanogels: an experimental and computational study, J. Mol. Liq. 362 (2022) 119716.
[61] C. Huang, R. Bai, T. Zhang, J. Wang, J. Yan, L. Peng, T. Yu, B. Han, Design of periodontitis vaccine: target, adjuvant, and delivery system, EngMedicine 2 (1) (2025) 100052.

Metal fluoride nanoregulators reverse therapeutic resistance via stemness remodeling to trigger pyroptosis for chemoimmunotherapy

Shumin Sun[1], Nailin Yang[1,2,*], Jihu Nie[1], Linzhu Zhang[1], Di Wang[1,3], Xingwei Sun[3,*], Yong Jin[3], and Liang Cheng[1,2,*]

[1]Institute of Functional Nano & Soft Materials (FUNSOM), Jiangsu Key Laboratory for Carbon-Based Functional Materials and Devices, Soochow University, Suzhou 215123, China.

[2]Macao Institute of Materials Science and Engineering, Macau University of Science and Technology, Taipa 999078, Macau SAR, China

[3]Department of Intervention, The Second Affiliated Hospital of Soochow University, Suzhou 215004, China

[*]Corresponding emails: lcheng2@suda.edu.cn; 20184133174@suda.edu.cn; nlyang@suda.edu.cn

Materials

Iron (II) acetylacetonate ($C_{10}H_{14}FeO_4$, 98%) and sodium fluoride (NaF, 99.93%) were purchased from Macklin Biochemical Technology Co., Ltd. Ammonium fluoride (NH_4F), sodium chloride, sodium bromide, sodium iodide, sodium phosphate, sodium carbonate, sodium selenide, sodium sulfide, and dibenzyl ether (95%) were obtained from Shanghai Aladdin Biochemical Technology Co., Ltd. Oleic acid (90%) and oleylamine (95%) were purchased from Beijing J&K Scientific Co., Ltd. 1, 2-dodecanediol ($C_{12}H_{26}O_2$, 93%) and 5-fluorouracil (5-Fu, 99%) were purchased from Tokyo Chemical Industry Co., Ltd. Dimethyl sulfoxide (DMSO, 99.5%) was obtained from Shanghai Lingfeng Chemical Reagent Co., Ltd. DSPE-PEG-NH_2 was purchased from Shanghai Ponsure Biological Technology Co., Ltd. All chemicals were of analytical grade and used without further purification. Anti-CD11c-FITC (Biolegend, clone N418, Catalog: 117306), anti-CD80-APC (Biolegend, clone 16-10A1, catalog: 104714), anti-CD86-PE (Biolegend, clone GL-1, catalog: 105008), anti-CD3-FITC (Biolegend, clone 17A2, catalog: 100204), anti-CD8-PE (Biolegend, clone 53-6.7, catalog: 100708), anti-CD45-Percp (Biolegend, clone 30-F11, catalog: 103130) were obtained from Biolegend and diluted at 1:300 for cell staining. Anti-CD44-FITC (ThermoFisher, clone IM7, catalog: 11-0441-82), anti-CD133-APC (ThermoFisher, clone 13A4, catalog: 17-1331-81) were purchased from ThermoFisher Scientific and diluted at 1:300 for cell staining. Adenosine Triphosphate (ATP) content assay kit (BC0300) was purchased from Beijing Solarbio Science & Technology Co., Ltd. Alexa Fluor 488 (AC18L032) was purchased from Shanghai Life-iLab Biotech Co., Ltd. Lactate Dehydrogenase (LDH) content assay kit (C0016) and mitochondrial membrane potential test kit (JC-1, C2006) were purchased from Beyotime Biotechnology Co., Ltd. GenScript YoungPAGE Precast Gels (M00928)

was obtained from GenScript Biotech Corporation. Fetal bovine serum (FBS, JYK-FBS-303) was purchased from Inner Mongolia Jin Yuan Kang Biotechnology Co., Ltd. Anti-calreticulin (CRT, catalog: 10292-1-AP), anti-high mobility group box 1 (HMGB1, catalog: 10829-1-AP), anti-DKK1 (catalog: 21112-1-AP), and anti-beta Catenin (β-catenin, catalog: 51067-2-AP) were purchased from Wuhan Sanying Biotechnology Co., Ltd. Anti-Cleaved Gasdermin D (N-GSDMD, catalog: 10137S), anti-Gasdermin D (GSDMD, catalog: 39754S), anti-cleaved caspase 1 (CC1, catalog: 89332S), and anti-α-tublin (catalog: 2125S) were obtained from cell signaling technology. GelNest™ Matrix (211352) was purchased from NEST Biotechnology Co., Ltd. Cell-culture dish (CCD06-100A) was purchased from Bioland. Confocal dish (1050001) was purchased from SAINING Biotechnology Co., Ltd.

Synthesis of the FeF_2 nanoparticles (NPs)

FeF_2 NPs were synthesized via a high-temperature thermal decomposition reaction based on our previous research[1]. 1 mmol of $C_{10}H_{14}FeO_4$, 2 mmol of NH_4F, 1.5 g of 1,2-dodecanediol, 1.5 mL of oleic acid, 1.5 mL of oleylamine, and 20 mL of dibenzyl ether were added into a 50 mL three-necked flask. Under stirring, the mixture was heated to 120 ºC for 15 mins, and N_2 was injected to remove water vapor and air. The mixture was subsequently heated to 280 ºC for 1 h to maintain the reaction. After being cooled to room temperature, the obtained FeF_2 was washed three times with cyclohexane and anhydrous ethanol. To enhance biocompatibility, FeF_2 was modified with DSPE-PEG-NH_2 in preparation for subsequent biological investigations.

Synthesis of the FFN-5

5 mL of FeF_2-PEG-NH_2 aqueous solution (75 μg/mL) and 5-Fu (125 μM) were added to a 50 mL round-bottom flask. Subsequently, the mixture was stirred at room temperature for 12 h. Remove the free 5-Fu via ultrafiltration, the obtained FFN-5 was washed three times with pure water. Store the product at 4 ^{o}C for further use.

Release behavior of 5-Fu from FFN-5

To evaluate the sustained-release performance of 5-Fu in FFN-5, 5-Fu was dissolved in pure water and diluted to different concentration gradients. Measure the absorbance value at 265 nm using an UV spectrophotometer. Utilize the scatter plot method to obtain the absorbance values for different concentration gradients of 5-Fu, plot the fitting line, and calculate the linear regression equation. To evaluate the pH-dependent release behavior of 5-Fu molecule from the as-prepared FFN-5, FFN-5 solutions was transferred to a dialysis tube and immersed in different buffer solutions (10 mL) at pH 7.4, 6.5, and 5.5. At designated time intervals, aliquots (0.5 mL) of dialysis solution were collected to measure the concentrations of 5-Fu by UV spectrophotometer.

Characterization

The morphology of the samples was characterized by transmission electron microscopy (TEM, FEITF20). Elemental mapping was performed by TEM (TALOS 200X). The chemical composition and crystallography of the samples were characterized by X-ray diffraction (XRD, Panalytical

Empyrean) with Cu Kα radiation (λ = 1.54056 Å). The concentration of Fe element was determined by inductively coupled plasma optical emission spectrometer (ICP-OES). Fourier transform infrared spectrometer (FT-IR) imaging was carried out by FT-IR Spectrometer (V70 & Hyperion 1000, Bruker, Billerica, USA). Zeta potential of the nanoparticles was recorded using MAL VERN ZEN3690.

The stability of FFN-5 under physiological conditions was evaluated by dispersing it in different solutions (FBS, PBS, RPMI-1640 medium, and 0.9% NaCl). Concurrently, photographic records of the solutions (0, 12, 24, and 48 h) and measurements of particle size changes were monitored.

Cellular experiments

Mouse colon cancer (CT26) cells were obtained from the Cell Bank, Shanghai Institutes for Biological Sciences, Chinese Academy of Sciences and cultured in a standard cell culture environment (37 ºC, 5% CO_2) with RPMI-1640 medium. A standard MTT assay was used to measure the relative cell viability after the incubation of CT26 cells with different treatments.

To screen the effects of various anions on stemness-related proteins, CT26 cells were exposed to various concentrations of diverse anions for a period of 24 h to extract protein, followed by an analysis of the changes in protein expression levels through western blotting and flow cytometry (FongCyte^{TM}, Challenbio).

To identify the optimal synthesis ratio of FFN-5, CT26 cells were co-incubated with varying concentrations of 5-Fu (0, 40, 60, 80, 100, and 200 μM) and different concentrations of FeF_2 (0, 10, 20, 40, 50, 75, and 100 μg/mL) for a duration of 24 h. Subsequently, the relative cell survival rate was measured using the standard MTT assay.

To investigate the mechanism through which F influences the Wnt signaling pathway, CT26 cells were incubated with varying concentrations of fluoride (0, 0.5, 1, and 2 mM) for 24 h. Subsequently, proteins were extracted from these cells. WB was then employed to analyze the expression alterations of phosphorylated β-catenin (p-β-catenin). In addition, a DKK1 inhibitor (WAY-262611, 3 μM) was co-incubated with CT26 tumor spheres for 24 h. Subsequently, proteins were extracted from these cells. WB was then employed to analyze the expression changes of DKK1 and β-catenin.

To assess the killing effect, CT26 cells were incubated with PBS, 5-Fu (50 μM), FeF_2 (75 μg/mL, based on the concentration of Fe), FFN-5 (75 μg/mL, based on the concentration of Fe) for 24 h. The relative cell viability was subsequently determined via the standard MTT assay.

For mitochondrial membrane potential detection, CT26 cells were incubated with PBS, 5-Fu (100 μM), FeF_2 (75 μg/mL), FFN-5 (75 μg/mL, based on the concentration of Fe) for 12 h. The cells were washed three times with PBS. Subsequently, the mitochondrial probe JC-1 was employed to stain the cell mitochondria for a duration of 30 minutes. The fluorescence was then detected via flow cytometry.

For the study of cell death morphologies, CT26 cells were incubated with PBS, 5-Fu (100 μM), FeF_2 (75 μg/mL), FFN-5 (75 μg/mL, based on the concentration of Fe) for 12 h. Subsequently, the cell morphology was observed through a fluorescence inverted microscope, and images were captured.

To evaluate the relative protein expression in vitro, CT26 cells were incubated with FFN-5 for 12 h. The CT26 cells were collected in 4 ºC cell lysis buffer for western blotting analysis. The protein concentration was calculated with a bicinchoninic acid (BCA) protein test kit. SD-PAGE was used to load and separate proteins. The proteins were then transferred to polyvinylidene difluoride (PVDF) membrane in a Tris-glycine transfer buffer and blocked with 5% bovine serum albumin (BSA) for 2 h

at room temperature. The membrane was incubated with primary antibodies (anti-GSDMD, anti-GSDME, anti-GSDMD-N, anti-GSDME-N, anti-cleaved caspase 3, anti-cleaved caspase 1, anti-DKK1, anti-β-catenin) at 4 ºC overnight. The membranes were washed and incubated with secondary HRP-conjugated antibody (anti-rabbit IgG) at 25 ºC for 2 h. The membranes were washed and imaged with a Gel Logic system (2200 Pro, Crestream, USA). The other groups included PBS, 5-Fu, and FeF_2.

To detect the activation of FeF_2-induced immunogenic death, the expression of CRT, the release of HMGB1, and the secretion of IL-1β, ATP and LDH were measured. After 6-8 h of various treatments (control, 5-Fu, FeF_2, FFN-5), the cells were blocked with 5% fetal bovine serum (FBS). which were then incubated for 1 h with anti-CRT or anti-HMGB1 primary antibodies and Alexa Fluor 488 secondary antibodies, followed by detection via flow cytometry. The secretion of IL-1β, ATP and LDH was measured by using IL-1β, ATP and LDH assay kits, respectively.

For the CT26 tumor sphere culture, an agarose base layer was prepared in 96-well plates, with 1×10^4 cells seeded into each well. The medium was partially refreshed daily while centrifuging at 1200 rpm for 5 minutes, a series of analyses can be performed.

For stemness analysis, the tumor spheres were transferred to a 12-well plate for cultivation and subjected to various treatments (control, 5-Fu, FeF_2, and FFN-5). For the immunofluorescence of OCT4, SOX2 and NANOG, the tumor spheres were stained with anti-OCT4, anti-SOX2, or anti-NANOG primary antibodies, and Alexa Fluor 488 secondary antibodies. All the images were acquired by confocal laser scanning microscopy. For the immunofluorescence of DKK1 and β-catenin, the aforementioned tumor spheres were collected and subjected to trypsinization, dissociating them into single cell. The collected cells were stained with DKK1 and β-catenin primary antibodies, and Alexa

Fluor 488 secondary antibodies, followed by detection via flow cytometry.

mRNA sequencing and analysis were conducted on CT26 cells from the control group and the FFN-5 group. Total mRNA was extracted from the cells using TRIzol reagent. After verifying the integrity and purity of the RNA, high-throughput sequencing of the mRNAs was performed at GENEWIZ Co., Ltd. Suzhou, China. The significant differential expression of genes was statistically analyzed by $\log2|FC| \geq 2$ and q value (FDR, p adj) ≤ 0.05. A p value ≤ 0.05 was considered to be significant for KEGG enrichment.

Tumor models

Female Balb/c mice (6-8 weeks) were purchased from Changzhou Cavins Biological Technology Co. Ltd, and all the animal experiments were conducted with the permission of Soochow University Laboratory Animal Center. For tumor inoculation, 50 μL of CT26 cell solution (PBS buffer, 2×10^6 cells) was subcutaneously inoculated into the back of each mouse to construct the tumor model.

Anti-tumor therapy in vivo

For NaF-enhanced chemotherapy, Balb/c mice, subcutaneously implanted with CT26 cancer cells, were randomly divided into the following four groups for various treatments once the tumor volume reached ~50 mm^3: (1) control, (2) 5-Fu (20 mg/kg, i.p.), (3) NaF (10 mg/kg, i.t.), and (4) NaF + 5-Fu. On days 0 and day 2, groups 3 and 4 were injected with NaF directly into the tumors, while on days 1, 3, 5, 7, 10, and 11, groups 2 and 4 were injected with 5-Fu via intraperitoneal injection. Tumor volumes

were calculated using the following formula: Volume = Length × Width^2/2. Moreover, the tumor tissues were collected after two days of various treatments for H&E and Ki67 staining to further assess the therapeutic efficacy after different treatments. All the images were acquired via CLSM.

For FFN-5 anti-tumor treatment, Balb/c mice, subcutaneously implanted with CT26 cancer cells, were randomly divided into the following four groups for various treatments once the tumor volume reached ~50 mm^3: (1) control, (2) 5-Fu (20 mg/kg, i.p.), (3) FeF_2 (10 mg/kg, i.t.), and (4) NaF + 5-Fu. On days 0 and day 2, groups 3 and 4 were injected with FeF_2 directly into the tumors, while on days 1, 3, 5, 7, 10, and 11, groups 2 and 4 were injected with 5-Fu via intraperitoneal injection. Tumor volumes were calculated using the following formula: Volume = Length × Width^2/2.

Moreover, the tumor tissues were collected after two days of various treatments for H&E and Ki67 staining to further assess the therapeutic efficacy after different treatments. All the images were acquired via CLSM.

Immune evaluation in vivo

CT26 tumor-bearing mice were treated according to the above methods and sacrificed after 7 days. Tumors were collected and cut into pieces to obtain single-cell suspensions. These cells were stained with fluorescence-labeled antibodies (DCs: CD11c-FITC, CD80-APC, and CD86-PE; T-cells: CD3-FITC, CD4-APC, CD8-PE, and CD45-Percp; CSCs: CD44-FITC and CD133-APC).

Combined immune checkpoint blockade (ICB) therapy for bilateral tumors

Twenty 6-8-weeks old female Balb/c mice were subcutaneously injected with 1 × 10^6 CT26 cells on the right side, which was regarded as the primary tumor. Then, the mice were subcutaneously injected with 5 × 10^5 CT26 cells on the other side to form distant tumors. When the primary tumors

grew to ~50 mm^3, the mice were divided into four groups: control, αPD-1, FFN-5 (i.t., 10 mg/kg), and FFN-5 (i.t., 10 mg/kg) + αPD-1. The primary tumors were injected with FFN-5. αPD-1 (20 μg/mouse) was intravenously injected on days 1, 3, and 5. The sizes of the tumors and the body weights were monitored every two days. Tumor volumes were calculated using the formula: Volume = Length × $Width^2/2$.

FFN-5 inhibited lung metastasis in vivo

5-Fu (100 μM) was added to the CT26 cells. Subsequently, the cells were co-incubated with PBS, NaF (1 mM, calculated based on F), and FeF_2 (1 mM, calculated based on F), respectively, for 24 h. After that, the cells were collected, and a CT26 cell suspension (in PBS, 1×10^5 cells) was injected via the tail vein. On the seventh day, the lungs of the mice were harvested for H&E staining.

Statistical analysis

The quantitative data were presented as mean values ± SD or mean values ± SEM, as indicated in the Figures. Statistical analyses were performed using GraphPad Prism or Origin software. P values calculated by the one-way ANOVA or two-tailed student's t-test are shown in the Figures. *$p < 0.05$, **$p < 0.01$, ***$p < 0.001$, and ****$p < 0.0001$.

References

[1] Q. Yu, S. Sun, N. Yang, Z. Pei, Y. Chen, J. Nie, H. Lei, L. Wang, F. Gong, L. Cheng, Self-Cascaded Pyroptosis-STING Initiators for Catalytic Metalloimmunotherapy, J. Am. Chem. Soc. 147 (2025) 3161-3173.

Supporting Figures

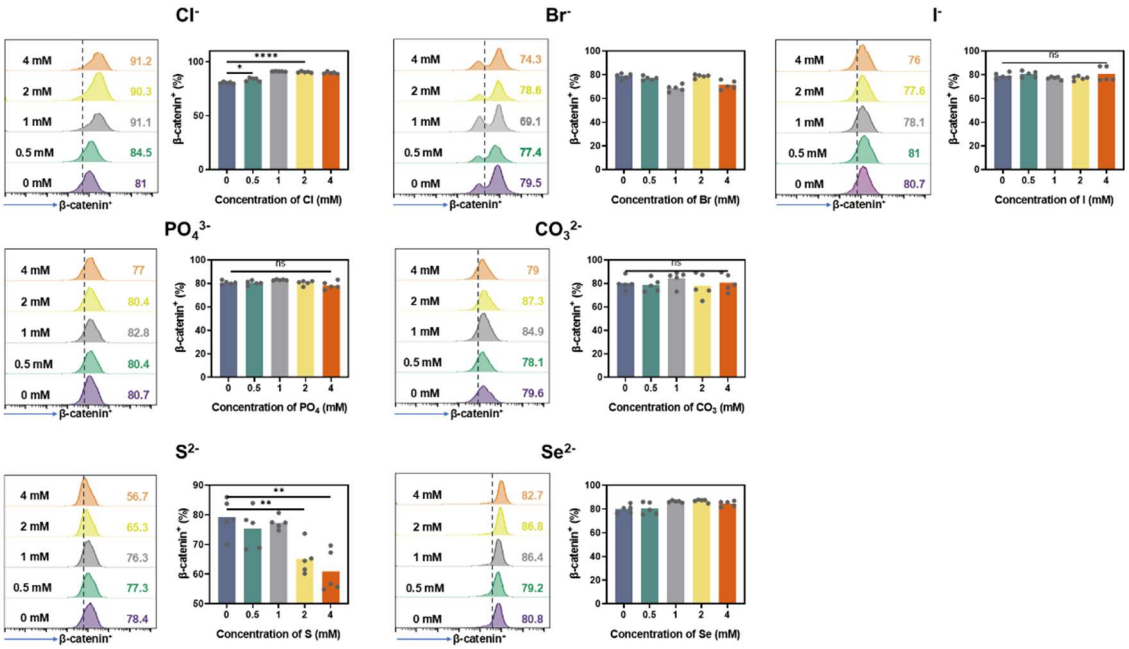

Figure S1. Flow cytometry analysis of β-catenin expressions following 24-h of incubation with various concentrations of different anions (Cl^-, Br^-, I^-, PO_4^{3-}, CO_3^{2-}, S^{2-}, and Se^{2-}) in CT26 cells.

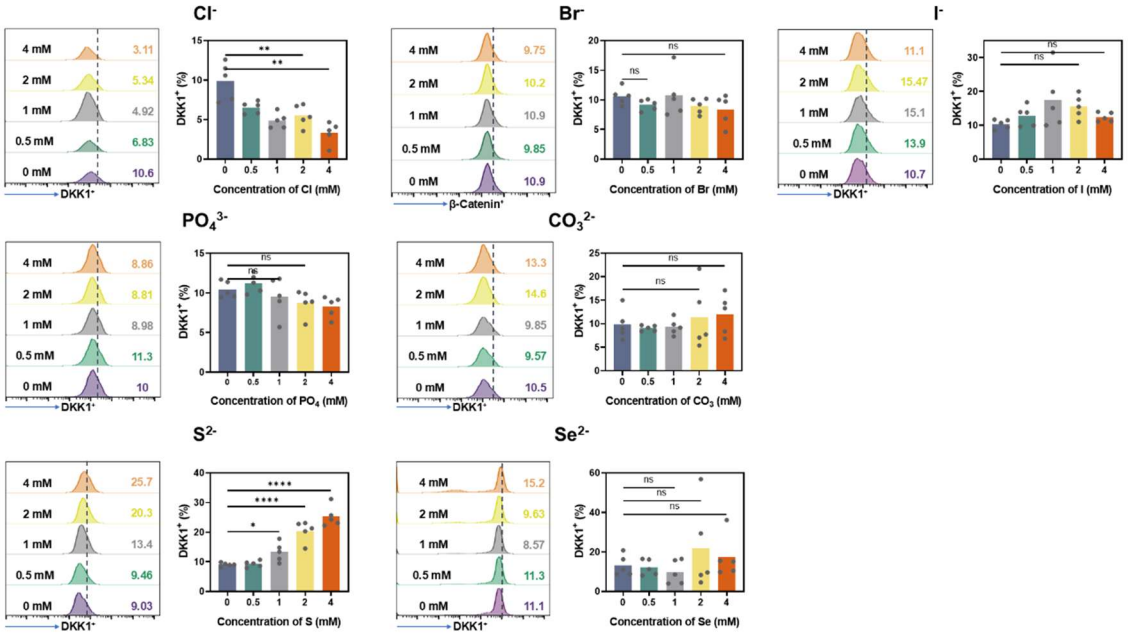

Figure S2. Flow cytometry analysis of DKK1 expressions following 24-h of incubation with various concentrations of different anions (Cl^-, Br^-, I^-, PO_4^{3-}, CO_3^{2-}, S^{2-}, and Se^{2-}) in CT26 cells.

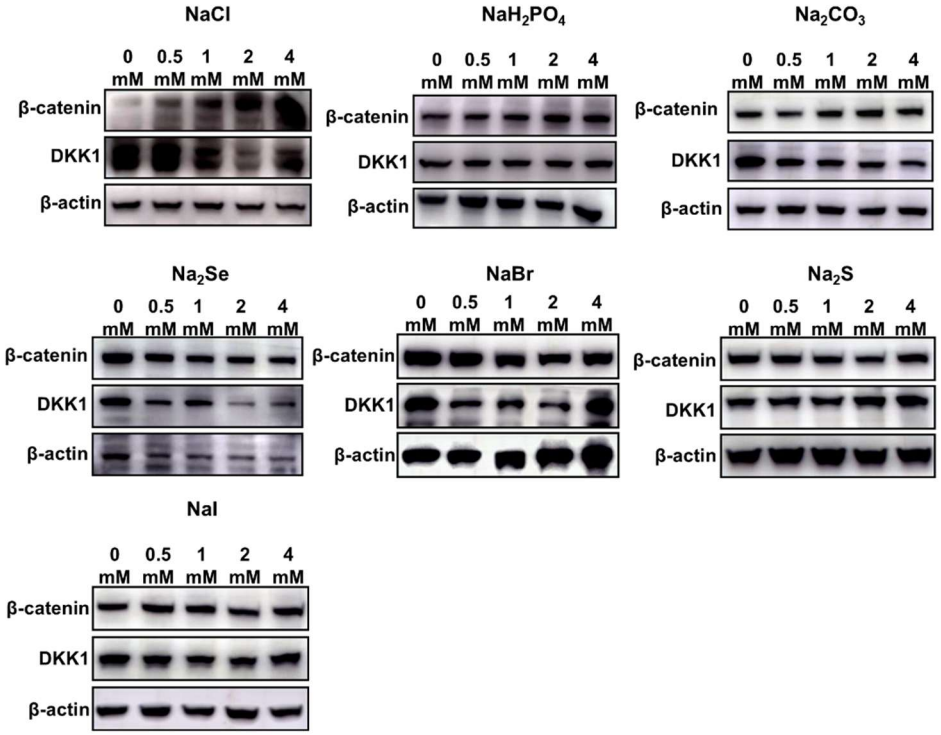

Figure S3. Western blot analysis of β-catenin and DKK1 expressions following 24-h of incubation with various concentrations of different anions (Cl^-, Br^-, I^-, PO_4^{3-}, CO_3^{2-}, S^{2-}, and Se^{2-}) in CT26 cells.

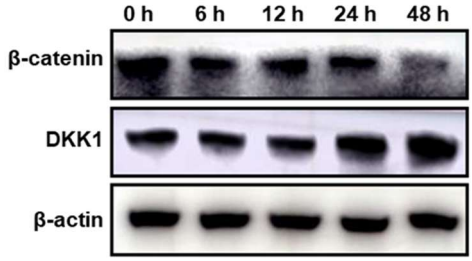

Figure S4. WB analysis the expression levels of β-catenin and DKK1 in CT26 cells underwent time-dependent changes following treatment with F^-.

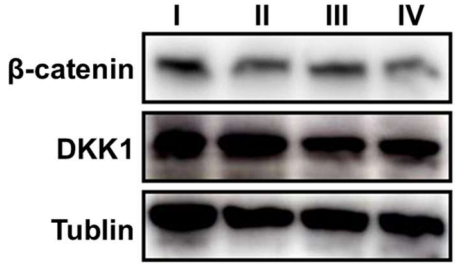

Figure S5. WB analysis of the expression levels of β-catenin and DKK1 in CT26 cells after different treatments. I: control, II: F^-, III: WAY-262611 (DKK1 inhibitor), IV: F^- + WAY-262611.

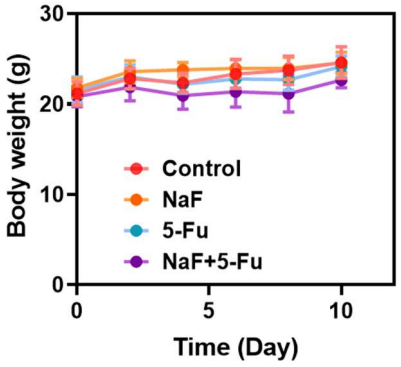

Figure S6. Weight changes of mice after different treatments.

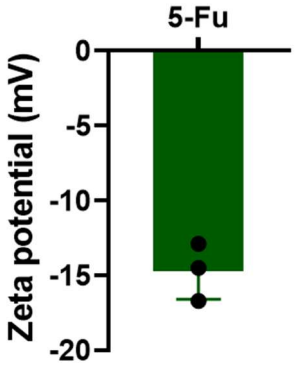

Figure S7. The zeta potential of 5-Fu.

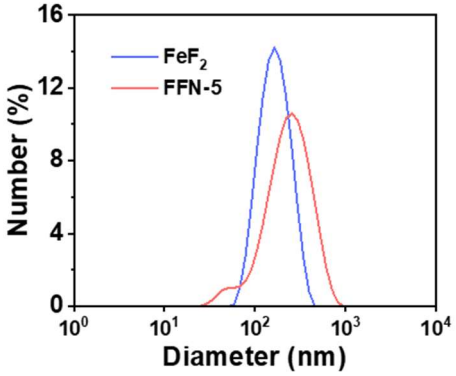

Figure S8. The hydrodynamic diameters of FeF_2 and FFN-5.

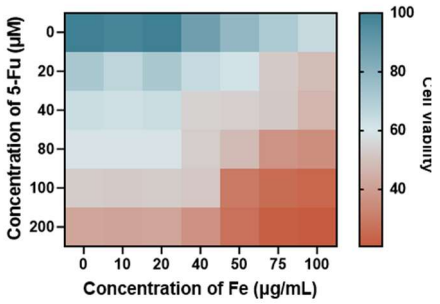

Figure S9. The survival rates of CT26 cells treated with a combination of different concentrations of 5-Fu and various concentrations of FeF_2.

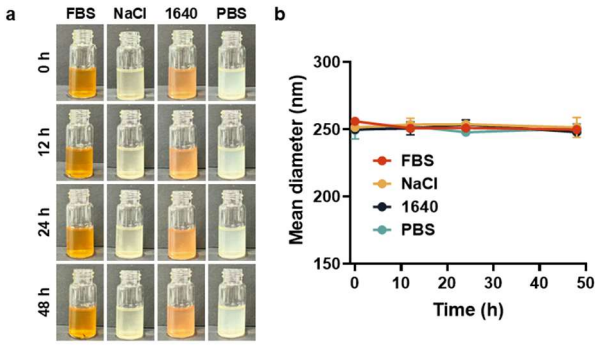

Figure S10. The images (a) and particle size changes (b) of FFN-5 over time in different solutions.

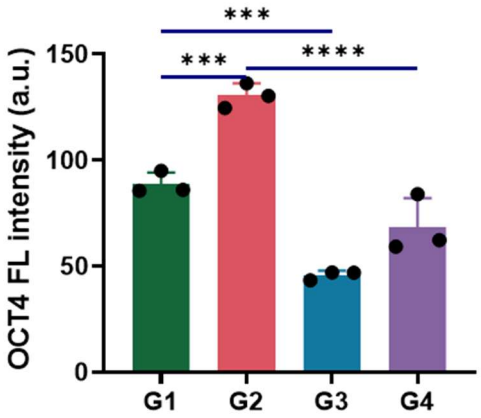

Figure S11. The fluorescence intensity statistics of OCT4 in CT26 tumor spheres following various treatments. G1: control, G2: 5-Fu, G3: FeF_2, G4: FFN-5.

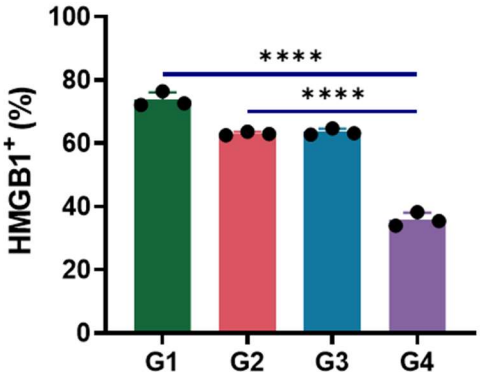

Figure S12. Statistical analysis of HMGB1 expression obtained from the flow cytometry analysis of CT26 cells. G1: control, G2: 5-Fu, G3: FeF_2, G4: FFN-5.

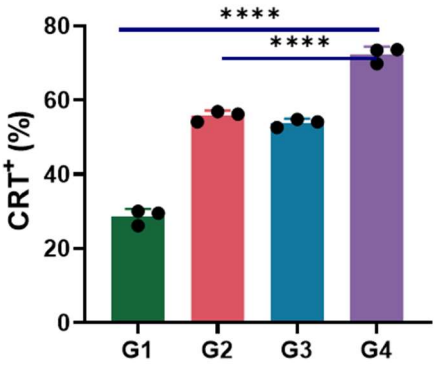

Figure S13. Statistical analysis of CRT expression obtained from the flow cytometry analysis of CT26 cells. G1: control, G2: 5-Fu, G3: FeF_2, G4: FFN-5.

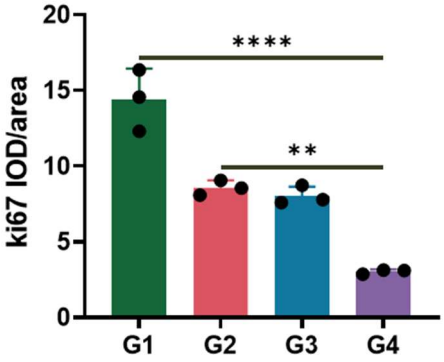

Figure S14. The integrated optical density (IOD)/area of ki67 in tumor slices after different treatments. G1: control, G2: 5-Fu, G3: FeF_2 and G4: FFN-5.

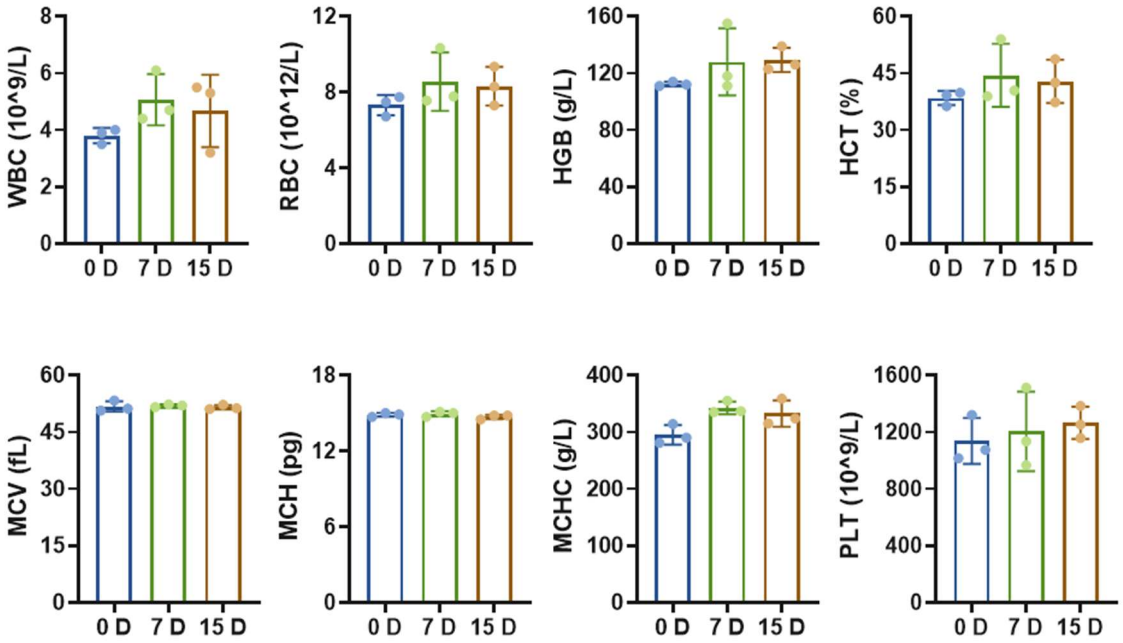

Figure S15. Hematological profiles of the mice treated with FFN-5 at various time points (0, 7, and 15 D). White blood cells (WBCs), red blood cells (RBCs), hemoglobin (HGB), hematocrit (HCT), mean corpuscular volume (MCV), mean corpuscular hemoglobin (MCH), mean corpuscular hemoglobin concentration (MCHC), and platelets (PLT).

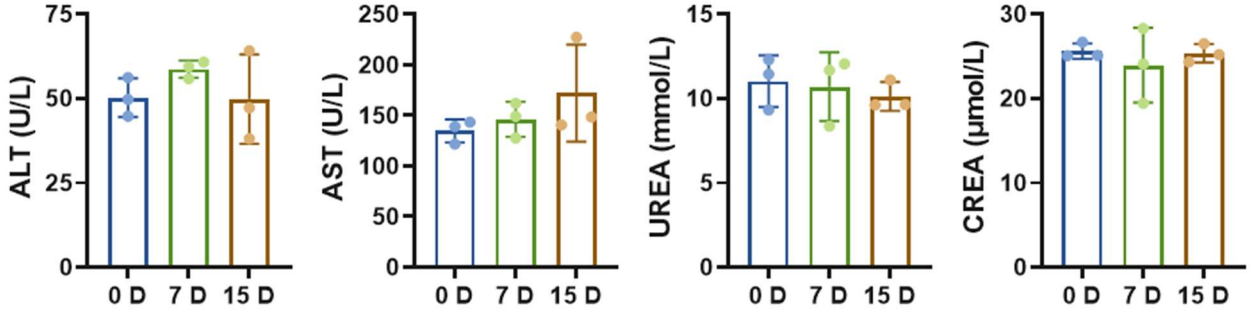

Figure S16. Blood biochemistry data of the mice treated with FFN-5 at various time points (0, 7, and 15 D). Alanine aminotransferase (ALT), aspartic aminotransferase (AST), UREA, and creatinine (CREA).

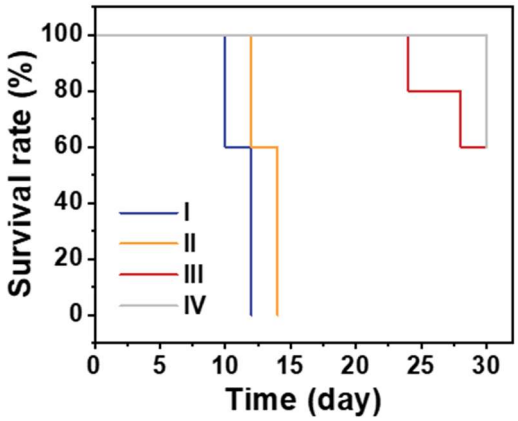

Figure S17. Survival curves of the mice after different treatments. I: control, II: α-PD1, III: FFN-5, IV: FFN-5 + α-PD1.

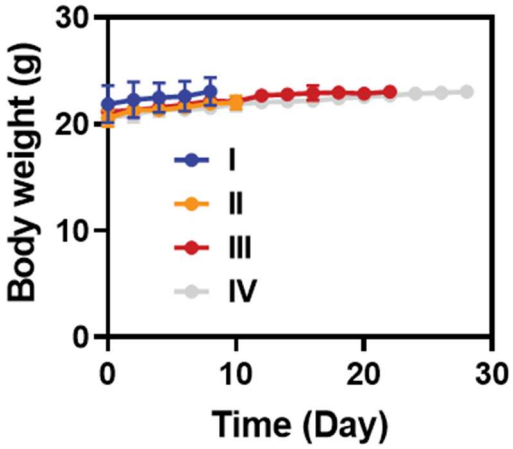

Figure S18. The changes in the body weights of the mice following various treatments. I: control, II: α-PD1, III: FFN-5, IV: FFN-5 + α-PD1.

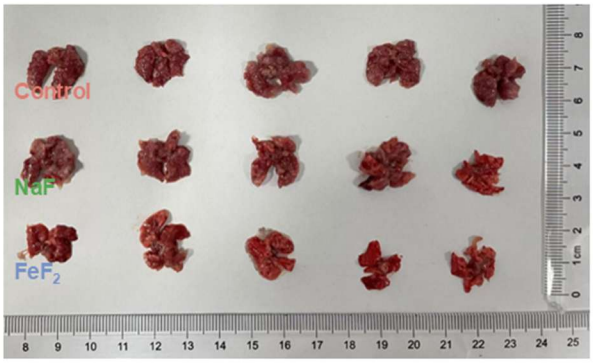

Figure S19. Photographs of the lungs taken from the mice after different treatments on days 7.